HAL open science

Past environmental and circulation changes in the South China Sea: Input from the magnetic properties of deep-sea sediments

C. Kissel, C. Laj, Z. Jian, P. Wang, C. Wandres, M. Rebolledo-Vieyra

▶ To cite this version:

C. Kissel, C. Laj, Z. Jian, P. Wang, C. Wandres, et al.. Past environmental and circulation changes in the South China Sea: Input from the magnetic properties of deep-sea sediments. Quaternary Science Reviews, 2020, 236, pp.106263. 10.1016/j.quascirev.2020.106263 . hal-02875152

HAL Id: hal-02875152
https://hal.science/hal-02875152

Submitted on 24 Jun 2021

HAL is a multi-disciplinary open access archive for the deposit and dissemination of scientific research documents, whether they are published or not. The documents may come from teaching and research institutions in France or abroad, or from public or private research centers.

L'archive ouverte pluridisciplinaire **HAL**, est destinée au dépôt et à la diffusion de documents scientifiques de niveau recherche, publiés ou non, émanant des établissements d'enseignement et de recherche français ou étrangers, des laboratoires publics ou privés.

HAL
archives-ouvertes.fr

Past environmental and circulation changes in the South China Sea: Input from the magnetic properties of deep-sea sediments

C. Kissel, C. Laj, Z. Jian, P. Wang, C. Wandres, M. Rebolledo-Vieyra

▶ **To cite this version:**

C. Kissel, C. Laj, Z. Jian, P. Wang, C. Wandres, et al.. Past environmental and circulation changes in the South China Sea: Input from the magnetic properties of deep-sea sediments. Quaternary Science Reviews, Elsevier, 2020, 236, pp.106263. 10.1016/j.quascirev.2020.106263 . hal-02875152

HAL Id: hal-02875152
https://hal.archives-ouvertes.fr/hal-02875152

Submitted on 24 Jun 2021

HAL is a multi-disciplinary open access archive for the deposit and dissemination of scientific research documents, whether they are published or not. The documents may come from teaching and research institutions in France or abroad, or from public or private research centers.

L'archive ouverte pluridisciplinaire **HAL**, est destinée au dépôt et à la diffusion de documents scientifiques de niveau recherche, publiés ou non, émanant des établissements d'enseignement et de recherche français ou étrangers, des laboratoires publics ou privés.

Version of Record: https://www.sciencedirect.com/science/article/pii/S0277379119310819
Manuscript_eb22e926ca66dc86fb656ecb9364c1de

Past environmental and circulation changes in the South China Sea: input from the magnetic properties of deep-sea sediments

C. Kissel[1*], C. Laj[2], Z. Jian[3], P. Wang[3], C. Wandres[1], M. Rebolledo-Vieyra[1,4]

1 – Laboratoire des Sciences du Climat et de l'Environnement/IPSL, CEA-CNRS-UVSQ, Université Paris-Saclay, Gif-sur-Yvette, France.
2 –Département de Géosciences, Ecole Normale Supérieure, PSL Research University, Paris, France.
3 - State Key Laboratory of Marine Geology, Tongji University, Shanghai, China.
4 –Now at : Independent Consultant, Chipre 5, SM 312, Mza 7, Benito Juarez, Quintana Roo, Mexico.

* Corresponding author: Catherine.kissel@lsce.ipsl.fr
Laboratoire des Sciences du Climat et de l'Environnement/IPSL, CEA-CNRS-UVSQ, Orme des Merisiers, Bat. 714, Université Paris-Saclay, 91190 Gif-sur-Yvette, France

Abstract

The South China Sea, located at the transition between the Pacific and the Indian Ocean, receives every year, mainly during the rain season, enormous amounts of river sediments originating from the erosion/weathering of rocks in the catchment basins. At sea, these sediments are carried by different water masses to their deposition site and they constitute a unique archive for past environmental studies in this region. The magnetic fraction of deep-sea sediments, though forming a minority in volume, provides incredibly valuable information for paleoceanographic reconstructions, as long as its provenance and source-to-sink processes are well constrained. After a brief description of the climatic, sedimentological and oceanographic context of the South China Sea (SCS), a review of the information available so far in the literature about the magnetic properties of SCS sediments is presented. It shows a large variety of interpretations/conclusions that finally results in a rather unclear picture. Because in such a context, the characterization of the sediment at the source is critical, the magnetic properties recently obtained from a set of samples from rivers and marine surface sediments are summarized to describe the present day situation. They are then used to interpret paleorecords from a set of seven marine cores distributed from the southern to the northern basins at different water depths and all covering at least the last climatic cycle.

The results reported here for the first time suggest that the magnetic mineralogy remains rather stable in time on land and that its time and spatial distribution at sea is an interplay of changes in sea level and deep-sea circulation. During low sea level periods, bottom deep-sea circulation is weak and the deposited sediment originates from the proximal rivers. On the contrary, during high sea level, the circulation is enhanced, transporting more sediment most likely from Taiwan and Luzon, to the northwestern part of the SCS and also, in smaller proportion, to the southern basin where it mixes with the local river-borne sediment. By comparing the two longest records, we observe that this pattern is repeated over the last 900 ka. Superimposed to the 100 kyr cyclicity we also observe a longer-term evolution with a maximum in the bottom current strength around 500 ka coinciding with global changes in the deep ocean circulation and carbon cycle. These new results based on a wide spectrum of magnetic properties of numerous marine sedimentary cores from the SCS show that the magnetic fraction yields important insights into past changes of the sedimentary pathways, in particular the dynamic of the deep-sea circulation, depending on the global climatic context.

Keywords: South China Sea, deep-ocean circulation, Environmental magnetism, hematite/magnetite, deep-sea circulation

Highlights (85 characters)

- Magnetic properties reveal interplay of sea level and deep oceanic circulation
- Low sea levels coincide with deposition of coarser magnetic grains
- Magnetic mineralogy documents interglacial active bottom current compared to glacial
- Long-term cyclicity is present with enhanced bottom circulation around 500 kyr.

1. Introduction

Low latitude regions play a critical role in climatic changes because they are the seat of the most active moisture and heat exchanges between the atmosphere and the ocean *via* the monsoon regime. Heat is redistributed by oceanic circulation and water mass exchanges (Wang et al., 2017). These processes are affected by the on-going climate change that induces cryosphere melting, ocean warming, changes in the evaporation/precipitation balance and sea level rise (Bindoff et al., 2013). This is particularly true in South East Asia and adjacent regions around the South China Sea (SCS), all located at the crossroad between Southeast Asian Monsoon and El Niño Southern Oscillation (ENSO) and on the path of the water masses from the Pacific to the Indian Oceans (Wang and Li, 2009). In order to better define the presently observed changes and to discriminate in the future those related to anthropic activities from the natural ones, the best possible description of the past climatic and oceanic changes is needed in this area.

Multi-proxy investigations conducted on both the biogenic and the detrital fractions of marine sediments from the SCS have shown that they are extraordinary archives of past environmental changes that affect not only the ocean but also the continents surrounding this extremely large semi-enclosed marginal sea (Wang and Li, 2009). Indeed, marine sediments recorded the interplay of East Asian Monsoon, surface and deep oceanic circulation and sea level. The difficult task is to decipher their respective influence.

For the continental climate, in particular changes in monsoon precipitations, vegetation changes were documented by pollen analyses (Sun et al., 1999; 2003; Wang et al., 2009) that also yielded information about the evolution of the northwestern shelf (Sun et al., 2003). Geochemical analyses of oxygen and carbon isotopes in planktonic foraminifera, coupled with Mg/Ca ratio, describe the surface water masses properties (e.g. Wang and Li, 2009 and references therein) despite the fact that oxygen isotopic ratios from planktic foraminifera in the SCS may be sensitive to the composition of the rain water (Wang et al., 2016). Apparent ventilation ages together with oxygen and carbon isotopic properties of benthic foraminifera showed that vertical mixing and advection from the Pacific Ocean were reduced during the last glacial maximum (LGM) compared to the Holocene (Wan and Jian, 2014; Wan et al., 2018). The SCS is among the few places around the world where information obtained from these "classical" geochemical, faunal and floral proxies can be completed by a large panel of investigations on the detrital part of the sediments. Indeed, the SCS receives about 700 x 10^6 tons/year of terrigenous material from the surrounding continents and islands (pre-dam values; Milliman et al., 1999). The terrigenous particles originate from areas with very different climatic, tectonic and geological context giving rise to different compositions which need to be first characterized at the sediment-source area.

Many analyses of the terrigenous content of marine sediments have been performed in the SCS (see i.e. Clift, 2015). However, the coverage of the entire system, starting from the characterization of the detrital sediment supplied by rivers, its storage in deltas and on shelves and its transport and deposition on the continental slope and in the abyssal plain has been rarely investigated. Clay mineralogy often coupled with Rare Earth Elements (REE) and magnetic mineralogy are the detrital tracers about which we have, so far, the largest knowledge in the modern SCS detrital environment.

The riverbed sediments are made of four clay mineral species: illite, chlorite, smectite and kaolinite (Liu et al., 2016 and references therein). Smectite is dominant in Luzon while it is very minor in other rivers. Among the three other species, illite and chlorite are dominant in Taiwan while they are in minor proportion and mixed with kaolinite in the Pearl River, Red River and Mekong. Kaolinite, in relatively high proportions in southern China and Indochina, dominates in the Malay Peninsula and Sumatra. Results from core tops differ from one study to another (Liu et al., 2013; 2016). In first approximation, smectite characterizes the area off

Luzon and the Gulf of Thailand while kaolinite is distributed along the coastlines off the Pearl River, around Hainan, off Vietnam and off Thailand. Illite and chlorite are dispersed south of Taiwan. In the central part of the SCS, the clay composition is quite uniform with 20% to 30% of each clay family (see Fig.8 in Liu et al., 2016). The use of this present-day clay mineralogy as a provenance indicator in paleorecords is still debated (Clift, 2015), due to the sensitivity of the clay minerals to changes in the continental erosion/weathering, including those related to human activities (Wan et al., 2015), which may have changed their nature/proportion at the source area in the past.

In his recent review of different proxies used to reconstruct the provenance history of the sediment deposited in the SCS, Clift (2015) did not consider magnetic properties as a possible tracer for sediment dispersal because their study was not yet enough developed in the SCS. However, magnetic properties, that have shown their potential to trace paleoenvironmental changes from different oceanic realms around the world (Kissel et al., 1999; 2008; 2009; 2013; Mazaud et al., 2002; Yamazaki and Ikehara, 2012), can potentially reveal interesting information in the SCS. Indeed, the physico-chemical properties of the magnetic particles produced in the different continental areas surrounding the SCS indicate that different magnetic minerals are present (Horng and Huh, 2011; Horng et al., 2012; Kissel et al., 2016; 2017). They reflect the nature of the parent-rocks, therefore depending on the geology of the river catchment rather than on the climatic conditions. The geographical distribution of the magnetic particles when deposited on the continental slope and in the abyssal plains reflects at present the magneto-mineralogical composition of the neighboring lands, although less contrasted (Kissel et al., 2018). This is true except for Taiwan where the sedimentary discharge is mainly linked to the typhoon activity (Liu et al., 2016 and references therein). The erosion is very active and the iron sulfides, eroded from the metasediments are transported by the rivers . At sea, however, these minerals are not stable and they transform into magnetite which, indeed is abundantly found south of Taiwan (Kissel et al., 2018).

In such a context, the diversity of the magnetic mineralogy on the geographical scale around the SCS can be taken as a positive basis. It constitutes a new efficient tool to better explore the provenance-transport-deposition path i.e. the processes by which the detrital sediment is dispersed after its delivery to the open sea depending on global and regional climate and oceanographic changes.

After a brief description of the climatic, sedimentological and oceanographic context of the SCS, we present here a review of the information available so far in the literature about the magnetic properties of SCS sediments. We then summarize the work accomplished over the past few years starting with the magnetic properties of river sediments and core tops, i.e. the present day situation. In order to use this knowledge to interpret paleorecords, we report here for the first time on results obtained from a set of marine cores distributed from the southern to the northern basins at different water depths. We then discuss the results in the frame of the general context of the SCS and of global oceanic circulation.

2. General context of the SCS

2.1. Present climatic setting

The monsoon climatic regime is the major demonstration of seasonal cycles in tropical regions. A large spectrum of evidences that monsoon is controlled by orbital parameters of the earth (in particular obliquity (41 ka) and precession (23 ka) as suggested by Clemens et al., 1991) is now available from the land and marine realms, although the regional-dependent phasing between the orbital forcing and the monsoon response is still debated (Clemens and Prell, 2007; Clemens et al., 2010; Kutzback et al. 2008). Recently, Wang et al. (2017) reviewed the different modern regional monsoons, clarifying their definition within the general system of global monsoon. In this context, the Southeast Asian monsoon system is quite unique, made of a tropical system (Western North Pacific monsoon) and a subtropical system (East Asian monsoon) extending as far as 50°N. In general, humidity transported during boreal summer from the Indian Ocean to the continent, results in heavy precipitations on land that is a major characteristic the East Asian Summer Monsoon (EASM). In winter, the Inter-Tropical Convergent Zone (ITCZ) migrates southward, towards Australia. A strong continental cold air mass over Siberia (Siberian high) induces northerly winter monsoon winds (East Asian Winter Monsoon, EAWM) giving rise to cold and dry climate in the northernmost area (Wang et al., 2017). The southernmost regions, located close to the Equator, receive high precipitations all year around under rather high and constant temperatures (26°C-27°C). The Eastern and Central Belts in the Malay Peninsula, the Barisan range in Sumatra and the Borneo mountains constitute obstacles for the Northeastern monsoon winds inducing heavy rainfalls and possibly increasing detrital discharges from November to February (Abdullahi et al., 2014).

2.2. Geological and Sedimentological setting

The amount and composition of the river-borne sediments are related to the climatic conditions prevailing in the catchment basins and also to both the nature of the eroded rocks and the tectonic activity.

Monsoon rainfalls induce conspicuous run-off and sediment discharges to the SCS, in particular from three Asian rivers which are among the largest in the world (Fig. 1): the Pearl River, the Red River, the Mekong River with 102, 138 and 166 Mt of suspended sediments per year, respectively (pre-dam values; Milliman and Farnsworth, 2011; Liu et al., 2016). Most of these rivers are now highly urbanized and industrialized at their mouth (M. Zhao et al., 2015).

The tectonically stable catchment of the Pearl River is made of limestones, granitic and sedimentary rocks. The Red River is much more incisive and is aligned with the active strike-slip Red-River Fault. The catchment of the river evolved with time and achieved its present state in the late Miocene (Wang et al., 2019). Sediments transported by the Red river originate from metamorphic complexes, sedimentary rocks and alluvium. The catchment basin of the Mekong River is submitted to extreme seasonal variations from the high eastern Tibetan plateau to the delta plain. The up-stream section, highly erosive through carbonate formations, low-grade metamorphic rocks and redbeds, contributes to about 50% of the total sediment transported by the river (Liu and Stattegger, 2014). In the lowlands, sediments resulting from the erosion of mainly sandstones and mudstones with several volcanic and granitic bodies are provided by tributaries incising the Khorat plateau and the Annamite mountains (Gupta, 2009; Panagos et al., 2011; Ridd et al., 2011; Thanh et al., 2019). About 8 kyr ago, the mouth of the Mekong was in Cambodia and since 6 kyr, it prograded seaward by about 250 km in southern Vietnam to form the present-day Mekong delta (Nguyen et al., 2000, Ta et al., 2002).

In the southernmost regions of the SCS, the mountain rivers from the Northeast Malay Peninsula also significantly contribute with about 35 Mt/yr to the yearly amount of sediments drained into the SCS through granitoids intruded by basaltic dykes, redbeds and marine limestones (Abdullah, 2009). The sediment delivery from Sumatra and Borneo to the SCS is not precisely known but on the basis of relatively small values reported for Sumatra rivers (Cecil et al., 2003) and for the two biggest rivers in Borneo (30 and 12 Mt/yr, respectively) (Staub et al., 2000; Hiscott, 2001), it is most likely significantly smaller, maybe by one order of magnitude, than that calculated from models (498 and 459 Mt/year, respectively; Milliman et al., 1999). The Sumatra rivers source in the Barisan mountains characterized by a pre-Tertiary basement interrupted by a range of active subduction-related volcanoes (Barber and Crow, 2009). They then flow through wide alluvial lowlands covered by clastic sediments, marine limestones and alluvium. In Southwest Borneo, the catchments of the rivers are mainly made of plutonic formations (granitoids and tonalites), sandstones, blackshales and shallow marine formations (Williams et al., 1988) while in central Borneo, argillaceous, arenaceous and calcareous sediments dominate with a few granodiorites in the eastern part of the basins (Staub and Esterle, 1992; Hutchison, 2005).

About 13 Mt/year of sediments, delivered during the wet season from the Luzon Island to the northeastern side of the SCS (Milliman and Farnsworth, 2011; Liu et al., 2016), are derived from igneous ophiolitic and basaltic rocks (Bachman et al., 1983).

In the north, the huge sediment discharge from Taiwan to the SCS is climatically controlled by both summer monsoon precipitations and typhoon occurrence and intensity. The rapid tectonic uplift of this region makes the mountain rivers highly erosive through the Central Range, the backbone of the island made of various types of metamorphic rocks in the greenshist facies (Horng et al., 2012).

2.3. Oceanic setting

Beyond the river deltas, part of the terrigenous sediments is deposited on the shelves (Szczuciński et al., 2009; 2013; Dung et al., 2013, Liu Y. et al., 2014; Ni et al., 2016; Zhong et al., 2017) while the rest reaches the open sea where the sediment is transported by the oceanic currents and deposited on the continental slope and in the deep basins (Wang et al., 1999). The circulation dynamic in the SCS, which acts as the main transport vector, is rather complex (Fig. 1).

The surface oceanic circulation is controlled by seasonal variations in the dominant wind directions related to EASM and EAWM (Wyrtki, 1961; Hu et al., 2000), monsoon-mountains interactions and additional influence from wind-stressed eddies (He et al., 2018). It is also influenced by the intrusion of the Kuroshio current through the Luzon strait which separates Luzon from Taiwan (Qu et al., 2000; Liu et al., 2008). The primary circulation consists of a basin-wide active cyclonic gyre dominating the surface current in winter. It corresponds to a strongly active southward coastal current along the Vietnamese and southern Chinese shores (Hu et al., 2000; Kuo et al., 2000; Zhu et al., 2016). In summer, the surface circulation is much weaker and gives rise to a northward directed coastal current. It is divided into two anticyclonic eddies located north and south of 12°N, separated by an active upwelling off Vietnam (Wyrtki, 1961; Kuo et al., 2000; Xie et al., 2003; Dippner et al., 2007; Zhang et al., 2014). Presently, cyclonic and anticyclonic mesoscale eddies form mainly along the northeastern part of the SCS and propagate along the northwestern boundary of the SCS (He et al., 2018). This propagation accelerates in winter compared to summer, and accounts for about 30% of the annual mean water transport across the Luzon strait (He et al., 2018).

Similarly to surface waters, deep waters are influenced by the connection with the Pacific Ocean through the Luzon strait in which the deepest channel reaches 2400 m. The western Pacific Deep Water (PDW), mainly derived from southern upper circumpolar deep waters (Kawabe and Fujio, 2010), passes over this strait, driven by the baroclinic pressure gradient across the strait (Qu et al., 2006). It then constantly fills the abyssal basin of the SCS, generating a basin-scale cyclonic deep boundary circulation and forming the Deep Water Bottom Current (DWBC) (Qu et al., 2006; Tian and Qu, 2012; Y. Zhao et al., 2015). Numerical simulations indicate that this cyclonic circulation is more active at 2500 m during summer time than during winter (Lan et al., 2015; Gan et al., 2016). Using sensitivity tests, the authors proposed that this seasonality is controlled by changes the deep-water overflow that may result from seasonal variations in the density difference described by Qu et al. (2006) between both sides of the Luzon strait. The residence time of the deep waters in the SCS is estimated differently depending on the authors, but in all cases, it is very short: between 30 years (Qu et al., 2006) and 70 years (Chang et al., 2010). The deep waters rapidly freshen (Chen et al., 2001) and upwell into upper layers, in particular forming the intermediate SCS water in summer (between 350 and 1350 m; Chen and Huang, 1996; Zhu et al., 2016). The latter is in turn exported out of the SCS through the northern part of the Luzon Strait (Liu et al., 2008 and references therein). The "sandwiched" vertical structure of the water column in the strait (Tian et al., 2006) is variable with sometimes only deep waters entering while surface and intermediate waters are both eastward directed, as observed in 2007 (Yang et al., 2010).

2.4. What about the past?

Paleoenvironmental changes in the SCS result from an interplay of monsoon intensity, position of the rain belt and sea level changes and oceanic circulation which in turn depend on the global circulation pattern.

In the past, the surface waters were sensitive to changes in both the monsoon intensity and the ice volume. The estimated sea surface temperatures (SST) decreased and the depth of the thermocline increased during glacial time compared to interglacials (Oppo et al., 2005; Steinke et al., 2006; M. Zhao et al., 2006). The surface circulation during glacial periods has been assumed to be similar to that of modern boreal winter season with a strong southward nearshore surface current while the interglacial circulation would mimic the present summer one with weaker northward surface currents (Wang and Li, 2009). At depth, the water dynamic is sensitive to the different properties of the Pacific water mass which flows through the Luzon strait and the source of which may change with time (Wang et al., 2011). Differences in radiocarbon ages of planktic and benthic foraminifera suggest that the deep SCS was less ventilated and the vertical mixing weakened during glacial time (Wan and Jian, 2014). Increased carbon storage is also observed in the more stratified glacial deep basin (Wan et al., 2018). This is still a debated subject as X. Zheng et al. (2016) argued, on the contrary, for a stronger bottom circulation with increased mixing and ventilation during the LGM and the Heinrich stadial 1 with respect to Holocene.

Since 1 Ma, the pollen composition changed synchronously with the oxygen isotopic record and showed that glacial (interglacial) periods correspond to enhanced winter (summer) monsoon (Sun et al., 2003). During glacial periods, the very wide and shallow shelves bordering the SCS on its western and southern part were partly or completely emerged. The distribution of the coastlines and the landmass configuration were therefore largely modified with respect to interglacials (Voris, 2000; Yao et al., 2009; Hanebuth et al., 2011). The glacial South China Sea was an almost entirely closed basin, the unique connection with the open ocean being the Luzon strait. Due to the gentle slope of the shelves, sea-level rise during deglaciation had very large transgressive effects on vegetation and sedimentation. Before Marine Isotopic Stage 6 (MIS6), while the Sunda shelf in the south remained stable (Voris, 2000), the shelf off the Pearl River was most likely much steeper than now, with a geographically reduced exposure during low sea-level stands (Sun et al., 2003).

The periodic regression/transgression and opening/closure episodes in/of the SCS obviously played a key role on the incisive character of the rivers, the vegetation pattern, the dynamic of the transport of the sediments and their distribution in the deep basins. A multi-proxy approach is best suited to address these questions and the magnetic properties of the marine sediments should now be considered as a possible tool.

3. State of art about magnetic studies in the SCS

Studies of marine sedimentary magnetic properties focusing on paleoenvironmental changes in the SCS developed slowly and progressively over the last 20 years. They aimed at reconstructing past changes in the oceanic circulation in the SCS and in the intensity of the monsoon. Articles dealing with surface and sub-surface sediments from the shallow continental shelves off the main rivers (Yim et al., 2004; Chen et al., 2009; Liu et al., 2010; Ouyang et al., 2013; 2017; Nguyen et al., 2016; Yang et al., 2008; Zhong et al., 2017) often reported only on the magnetic susceptibility as an easy-to-measure and non-destructive proxy for the total magnetic content (Yim et al., 2004; Liu et al., 2010; Chen et al., 2009; Zhong et al., 2017). The general pattern deduced from these measurements is a systematic decrease in this parameter from the present coastlines to the open sea (Liu et al., 2010; Ouyang et al., 2017; Zhong et al., 2017) with highly different values depending on the geographical area and on the sediment grain size (Liu et al., 2010). However, because this parameter reflects both para- and ferro-magnetic (*s.l.*) content and it is sensitive to different mixtures of magnetic minerals and grain sizes, its interpretation may be difficult without complementary magnetic analyses. For example, the higher susceptibility values obtained from surface and sub-surface sediments compared to the older ones in the Hong-Kong bay may indeed reflect contamination related to the harbor activity (Yim et al., 2004) but also the presence of superparamagnetic grains (Ouyang et al., 2013; 2017) or diagenetic iron sulfate reduction linked to the high methane content (Yim et al., 2004; Yang et al., 2008; Chen et al., 2009).

Because deltas and shelves give only access to Holocene sediments, most of the paleo-records are obtained from the continental slope and the deep basins (Table 1; Fig. 1). Unfortunately, part of the information and data are of difficult access for the international community because many papers are only written in Chinese.

The first article reporting on magnetic properties in the northern SCS was based on a long sedimentary sequence taken during the ODP leg 184 (site 1146, Fig. 1) and covered the last 1.18 Ma (Kissel et al., 2003). A very significant and progressive decrease in the magnetic concentration (magnetic susceptibility κ; anhysteretic (ARM) and isothermal (IRM) remanent magnetizations), together with a general increase in the magnetic grain size and coercivity between 1.18 to 0.7 Ma was interpreted as a progressive decline of the EASM intensity during the mid-Pleistocene transition. A following and enhanced EAWM period was proposed to explain the weak magnetic content made of relatively coarse magnetic grains between 0.7 and 0.2 Ma. Since 0.2 Ma, a general increase in concentration, decrease in coercivity and fining in magnetic grains are likely related to a progressively wetter climate. Superimposed on this long-term pattern, changes in the magnetic grain size were observed at the orbital scale with fine (coarse) magnetic grains quasi-systematically related to warm (cold) periods. This was attributed to variations in the intensity of the East Asian monsoon and alternations of chemical weathering (warm)/physical erosion (cold).

This paper remained for a long time the only one reporting on magnetic properties of sediments from the deep SCS. For the last 400 ka, it has recently been completed by the more detailed study of the nearby core MD12-3432 (Table 1; Fig. 1) located about 900 m deeper, in the same deep water mass (Chen et al., 2017a, b). The clear coarsening of the magnetic grains during glacial periods was confirmed and it is associated to coarser sediment as documented by sortable silt studies, more kaolinite and a higher sedimentation rate. The degree of low-field magnetic anisotropy illustrates compaction of the planar-parallel coarse magnetic minerals rather than a better alignment of elongated grains by bottom currents (Chen et al., 2017b). Therefore, changes in magnetic grain sizes and mean sortable silt were attributed to the glacial lowering of the sea level, making the site more proximal to the source. This is consistent with the coeval increase in kaolinite content which characterizes the Pearl River sediments and which settles close to the river mouth due to its flocculation properties. Superimposed to these 100 ka oscillations, 23 ka precession fluctuations were observed in this core: high coercivity minerals and fine sortable silt which coincide with precession minima were attributed to enhanced eolian transport during weak EASM periods also marked by low smectite/(illite+chlorite) ratio (Fig. 6 and 8 in Chen et al., 2017a).

At shallower depth, on the continental slope off the Pearl River, Yang et al. (2016) observed two rather abrupt changes in the composition of the magnetic fraction around 40 kyr and 15 kyr (core STD111; Table 1; Fig. 1). From 84 kyr (the bottom of the core) to 40 kyr, the high fluxes of magnetic particles in particular hematite and maghemite together with a high chemical index of alteration (CIA) is interpreted as resulting from strong chemical weathering processes on the continent. At the same time, coarser magnetic particles are attributed to intensified erosion and more efficient river transport. Around 40 kyr, a significant decrease in both the terrigenous input and the chemical weathering is interpreted as related to a weaker monsoon intensity (Yang et al., 2016). Finally, since 15 kyr, the same situation as before 40 kyr prevailed with, however, less hematite.

The period between 36 kyr BP and present was also studied by Li et al. (2018) on a core located southward, off the paleo-mouth of the Red River (PC338, Table 1, Fig. 1). A turbidite, emplaced during the lowest sea level period when exposed slopes were unstable, interrupts the recording of the paleoenvironmental changes between 25 and 20 kyr B.P. In this core, the hematite content is high during LGM (S-ratio ~ 0.7) and decreases during H1, together with sedimentation rate, magnetic concentration (κ, ARM, IRM) and grain size (detrital and magnetic one) (see Figure 7; Li et al., 2018). Due to the location of this core, this is attributed by the authors to the low sea level bringing the mouth of the Red River closer to the site. In addition, cold and dry climate prevailed during LGM and H1 and the enhanced winter surface coastal current and vegetation changes promoted magnetic mineral deposition. After 15 kyr BP, the cold and dry Younger Dryas period had magnetic characteristics different from those observed during LGM and H1 because of higher sea level modifying the sediment transport path.

Very little information was retrieved from the magnetic parameters on ODP site 1144, located right in the core of the sediment drift (Table 1; Fig. 1; Hu et al., 2012). Only a broad increase in the hematite/goethite ratio obtained by diffuse reflectance spectroscopy (DRS) between 11 and 7.5 kyr was observed, in phase with a general fining of the sediment. The magnetic grain size (not discussed and not shown but reported in Table 6 in Hu et al., 2012) also shows a broad fine grains event between 11.5 and 7.5 kyr BP. Together with finer sedimentary grains and other weathering proxies, this early Holocene event was interpreted as resulting from monsoon intensification and reworking of sediments first deposited on the shelf and oxidized during the low sea level stands of the LGM. A coeval broad fining was also observed by Zheng et al. (2016) in the magnetic grains of a core located up-stream with respect to ODP site 1144 (core 10E23; Table 1; Fig. 1). However, this was not interpreted in term of monsoon but as a “pulse of intensification in the deep current”.

Using a low-resolution age model during the Holocene period for a core located at much greater depth (core PC24; Table 1 and Fig. 1), Ouyang et al. (2016) concluded that increase in magnetic concentration and magnetic grain size indicate a warm middle Holocene climate (7.3 to 3.5 kyr) with more humid conditions between 6 and 3.5 kyr. Warm and wet climate would have prevailed again over the last 2.5 kyr. This core has a similar sedimentation rate during the Holocene, even slightly higher, than core PC338 in which Li et al. (2018) also used the magnetic properties as climatic tracers. However, the observations are very different and the interpretation of the magnetic parameters are even opposite at the two sites. The rather uniform magnetic grain size in core PC338 during the Holocene is quasi periodically interrupted by short events with coarse magnetic grains attributed by the authors to dry climate, increased EAWM, low precipitations (low weathering) and enhanced winter currents. Such short events are not observed in core PC24 where quite long periods characterized by coarse magnetic grains are interpreted as related to humid climate (high precipitation rates inducing high run-off). The detrital sources of these two cores are most likely different but such a climatic contrast on land is not expected during the Holocene in the neighboring regions.

On shorter-time scales over a longer time interval, stronger bottom currents are suggested during cold abrupt events (Younger Dryas, LGM and Heinrich events 1 to 11) on the basis of a higher degree of magnetic anisotropy and coarser magnetic grains (core 10E23; Zheng et al., 2016). On the basis of coarser sortable silt grains and maximum axes of anisotropy ellipsoid parallel to the local bathymetry in cores PC83 and PC111, Li et al. (2019) reached the same conclusion. However, no coarsening of the magnetic grains was observed (Yang et al., 2009) and in any of these studies, local sedimentary processes can be excluded based on the orientation of the elongated magnetic grains (Chen et al., 2016).

Finally, in the southern basin of the SCS, only two sites have been studied. In one of them, that we also investigate below (ODP 1143; Table 1; Fig. 1), the hematite/goethite ratio (DRS measurements) used as a paleo-precipitation proxy is higher (lower) for dry (wet) conditions (Zhang et al., 2007). The authors describe very long-term changes that they attribute to ENSO variability. On this basis, they argue that a control of EASM by orbital forcing at the glacial/interglacial time scale may be invalid. Over the last climatic cycle, the most prominent feature in the record is a significant decrease of the hematite/goethite ratio over the two last deglaciations suggesting changes from dry to wet climate in the Mekong basin. The other core (86GC; Table 1; Fig. 1), located NW of the ODP site 1143, ranges from 32 kyr to present and therefore covers the LGM and the deglaciation (Ouyang et al., 2014a). The changes in the Holocene/glacial magnetic content with more (less) magnetite, less (more) hematite are interpreted as reflecting redox changes in the source area and fine/coarse magnetic grains as illustrating different transportation paths and distances to the site.

The various magnetic analyses performed on long marine cores from the SCS and the interpretation made by the authors are summarized in Figure 2. The final results are expected to differ depending on the geographical location of the cores, their water depths and also the sedimentation rate. However, the set of analyzed magnetic properties and the deduced conclusions are much more complex and variable from one study to another resulting in a very unclear final picture (Fig. 2). For example, the magnetic grain size is interpreted sometimes as a bottom current strength indicator (core 10E23), sometimes as a sea level proxy (MD12-3432) or as illustrating wet/dry conditions (core PC24, PC338). Also, the use of the anisotropy of magnetic susceptibility as a bottom current strength indicator, if simple in theory, is rather complicated to apply to natural deep-sea environments: orientation of the maximum axes may indicate bottom current orientation (10E23; PC83 and PC111) or direction of terrigenous delivery from land (STD111; MD12-3432). Also, the platy clay minerals carry part of the magnetic susceptibility but their role in the compaction and shape of the anisotropy ellipsoid is largely ignored. The real and complete description of the magnetic fabric is not always made on the basis of all the intensity ratios proposed in the literature and which should be combined to better describe the shape of the anisotropy ellipsoid (Tarling and Hrouda, 1993). Finally, the interpretation of the magnetic parameters is also based on the comparison with other proxies which are different from one study to another.

In such a semi-closed basin, the magnetic properties of marine sediments are not only dependent on the climatic and oceanographic context but also, and overall, on the composition of the river-borne sediments. Although the latter may have changed in the past, depending on the source area and the climatic conditions on land, their present characterization is a significant step forward for the understanding of paleo-records. In order to be able to make use of this information, a systematic study of a wide range of magnetic parameters has been conducted in each river system significantly feeding the SCS. This includes of course the three main Asian rivers that are the Pearl River, the Red River and the Mekong rivers (Kissel et al., 2016) and the mountain rivers distributed in the Malay Peninsula, Sumatra, Borneo, Luzon and Taiwan (Kissel et al., 2017). In all these rivers, the most efficient mobilization and transport of sediment occur during the rainy season when water level and water turbulence are high. Intra-basin minor variations are often related to the local geology because the properties of the magnetic fraction illustrate the lithology and the degree of weathering of the parent rocks.

At the inter-basin scale, the average magnetic properties are variable from one river basin to another and a clear difference is observed between the northern and the southern part of the SCS (Fig. 3). In the northern regions, magnetite is abundant in the Pearl River and in Luzon and it does not allow to discriminate between the two sources. However, the analyses of surface sediments have shown that Luzon is a much bigger contributor delivering to the sea magnetite in concentrations about 10 times larger than that found off the Pearl River (Kissel et al., 2018). Taiwan rivers, on the other hand, are characterized by large amounts of pyrrhotite although not always clearly found at sea (Kissel et al., 2018). Hematite is significantly more important in volume in the southern sediments (except for Sumatra and SW Borneo) than in the northern ones with an intermediate composition of the Red River sediments where magnetite and hematite are mixed. The higher hematite contribution to the total magnetic signal in the southern regions gives rise to the weak magnetic bulk values previously obtained. At sea, the north-south magnetite/hematite gradient exists in the composition of the surface sediment but it not as contrasted as on land (Kissel et al., 2018) (Fig. 3).

The North-South magnetic mineralogical differences observed in the fluvial sediments reaching the SCS and their distribution in the deep-basins is a robust requirement to better decipher marine records of past environmental changes.

4. New magnetic records from the SCS

4.1 Sedimentary sequences and age models

Over the last 20 years, several coring operations have been conducted in the SCS in particular by the R.V. *Marion Dufresne.* A number of long piston CALYPSO cores doubled by gravity CASQ cores (labeled Cq) were collected. In a general way, at each site, we produced a composite record, privileging the undisturbed CASQ core for the top first meters and completing it at greater depth by the CALYPSO sequence. The correlation between the two is usually based on the magnetic susceptibility records.

During the Marco Polo cruise in 2005, the cores were distributed along a South-North transect at different water depths (Laj et al., 2005). They are examined here, completed by one core taken during the Wepama cruise in 2001 (Bassinot and Baltzer, 2002) and by cores taken in 1999 during the ODP Leg-184 (Wang et al., 2000).

The studied sites can be divided into three groups based on their geographical and depth distribution (Fig. 1; Table 1). The first group, labeled "southern" group, between 8.8°N and 10.5°N is formed, from the shallowest to the deepest, by cores MD01-2393, MD05-2896Cq/2897 and ODP site 1143. The "central" group around 14°N is composed of cores MD05-2900Cq/2901 and MD05-2898Cq. Finally, the "northern" group, around 19°N is made of ODP sites 1145 and 1147.

Oxygen isotope stratigraphy used to construct their age models is already reported in various articles (Suppl. Fig. S1). We focus here first for all the cores on the last climatic cycle (back in time to MIS6 at about 160 kyr) before considering the longest records covering the entire Brunhes period.

For the southern group, the chronology of core MD01-2393 is based on radiocarbon dating and planktonic oxygen isotope record (*G. ruber* (white); Liu et al., 2004). Additional tie points were constituted by the last occurrence of *G. ruber* (pink) during termination II and the youngest Toba ash layer. At the time of the publication, the age of the latter was 74 ± 2 kyr (Ninkovitch et al., 1978) but we changed it to its most recent evaluation at 75 ± 0.9 kyr (Mark et al., 2013). The age models of ODP site 1143 and of cores MD05-2896Cq/97 are based on benthic foraminifera record tuned to obliquity and precession records with a 8 kyr and a 5 kyr lag, respectively (Tian et al., 2002; 2010; Huang and Tian, 2012; Wan and Jian, 2014; Dong et al., 2015). The Toba ash layer is also well expressed in these cores (Bühring et al., 2000). In core MD01-2393, it could not be sampled because it corresponds to a small break in the core.

In the central group, core MD05-2901 was dated using planktonic oxygen isotope record (*G. ruber* (white); Li et al., 2009). It has been damaged during coring between 13.6 and 14.5 m because of localized weakness of the liner (Laj et al., 2005). This corresponds to the period between 136 and 150 kyr (see below), an interval unfortunately not covered by the twin CASQ core (MD05-2900Cq). The benthic oxygen isotope data from *C. wuellerstorfi* from core MD05-2899 (Wang et al., 2016) were transferred to the twin core MD05-2898Cq. The northern group was dated using oxygen isotopes from benthic foraminifera (Oppo and Sun, 2005; Tian et al., 2008).

The average sedimentation rates of all these cores vary between about 6 and 24 cm/kyr (Suppl. Fig. S1; Table 1).

4.1 Sampling and magnetic parameters

All the studied cores were sampled using u-channels (2 x 2 x 150 cm) (Weeks et al., 1993) pushed in the center of the half core (or of the CASQ core on board), free of any shearing, smearing, or distortion that may be induced during coring. Cubic samples (2 x 2 x 2 cm) were also taken at specific horizons for 3-axes IRM thermal treatment (see below).

Laboratory analyses of the magnetic properties were made at the Laboratoire des Sciences du Climat et de l'Environnement (LSCE). The laboratory procedures are described in detail in the supplementary information and we just give here an overview of the use of the different parameters. They are also summarized with their meaning in Table 2.

Concentration in magnetic particles was evaluated using the volume low-field magnetic susceptibility (κ), the Anhysteretic (ARM) and the Isothermal (IRM) Remanent Magnetizations. Possible mineralogical mixtures were detected by examining the resistance of ARM and IRM to the alternating field (AF) demagnetization. It was evaluated using the median destructive fields MDF_{ARM} and MDF_{IRM} values and the percentage of magnetization still present in the sample after demagnetization at 80 mT ($\%ARM_{@80mT}$ and $\%IRM_{@80mT}$). The 0.3T back field ($IRM_{-0.3T}$) applied after the IRM at 1T (IRM_{1T}) allowed to calculate the S-ratio (= $-IRM_{-0.3\,T}/IRM_{1T}$) (King and Channell, 1991) illustrating the ratio of low to high coercivity minerals.

Thermal demagnetizations of 3-axes IRM (Lowrie, 1990) were conducted on the cubic samples taken at specific key horizons determined on the basis of the u-channel study. The cubes were taken alongside the u-channels. We checked that the magnetic properties of these discrete samples (κ; ARM, IRM, MDF_{ARM}, MDF_{IRM}, S-ratio) were virtually identical to those of the equivalent horizons in the u-channels. This confirmed that no error was made in the respective stratigraphic heights of the cubes with respect to the u-channels. For the ODP cores 1143 and 1145, we only had the u-channels from which we extracted cubes. Because the last measurement made on the u-channels was the stepwise demagnetization of a $IRM_{@1T}$, the cubes could be submitted again to 1T (the first of the 3-axes IRM) for the thermal demagnetizations of 3-axes IRM. Sediments from ODP core 1147 were not available anymore for this experiment. By examining the thermal decay rate of each component, this experiment allowed us to attribute a Curie (Néel) temperature or a transformation temperature to each coercitive family identified by the previous measurements. The magnetic mineralogy could therefore be determined.

Magnetic grain size was approached by comparing ARM, IRM and κ at each measured horizon using the empirical relationship between these parameters, valid for magnetite (Banerjee et al., 1981; King et al., 1982). Small amounts of sediment were also taken at regular intervals in all cores to measure the magnetic hysteresis parameters. They were used to determine the domain state related to the magnetite grain size (Day et al., 1977; Dunlop, 2002). High resolution IRM acquisition curves were also decomposed in Cumulative Log

Gaussian (CLG) components (Kruiver et al., 2001) in order to determine the different coercivity families.

5. Results

5.1 bulk magnetic parameters

The bulk magnetic parameters, κ, ARM and IRM are reported in Figure 4. The average values as well as the maximum and minimum values of these parameters are reported in Table 3 for each core. In the southern and central areas, the three parameters vary by a factor of 2 to 4 (Fig. 4a-e). The Toba ash layer is very prominently marked in cores MD05-2896Cq-97 and ODP site 1143 by high IRM and κ values and low ARM values (Fig. 4b-c). In ODP sites 1145 and 1147 from the northern group, the variations of κ, ARM and IRM have significantly greater amplitudes (Fig. 4f-g; Table 3).

Besides these first order variations, differences exist between the different parameters in each core and they likely illustrate local variations in magnetic mineralogy, magnetic grain size and/or magnetic concentration (or concentration of one magnetic fraction with respect to another one).

Except for the Toba ash layer, which is composed of very low coercivity magnetic minerals with an ARM median destructive field (MDF_{ARM}) of 15 mT, all cores are characterized by MDF_{ARM} ranging between 24 and 38 mT with a great majority between 30 and 35 mT (Table 3) and a full demagnetization at 80 mT ($\%ARM_{@80mT} < 6.5\%$; Table 3). This indicates that low coercivity minerals are present everywhere and dominate the magnetic bulk parameters.

5.2 Magnetic mineralogy

The median destructive field of IRM (MDF_{IRM}) is more variable than that of ARM. The average values are around 33-34 mT in the south, around 28 mT in the center and around 18-20 mT in the north (Table 3). Also, the percentages of IRM remaining after demagnetization at 80 mT ($\%IRM_{@80mT}$) vary between 4 and 29% with the highest ones in the south. These parameters reflect the variable presence of high coercivity minerals, which may be dominant in volume and mixed with low coercivity ones. This is confirmed by the S-ratio which has a similar pattern in each group with variable amplitudes, ranging between 0.7 and 1 in the entire dataset (Fig. 5). Because of their low characteristic magnetization, the high coercivity minerals are difficult to extract from the population of strongly magnetized low-coercivity ones. Therefore, in order to clearly identify the magnetic minerals present in the cores, we analyzed the thermal spectrum of each coercivity family, using cubic samples collected at horizons corresponding to almost each maximum and minimum of the S-ratio.

Examples of 3-axes IRM thermal demagnetizations are shown in Figure 6a-c and results are reported for all the samples in Figure 6d as the percentage of IRM remaining at 600°C ($IRM_{xT@600°C}/IRM_{@20°C}$) versus the contribution to the total IRM at room temperature ($IRM_{xT@20°C}/IRM_{@20°C}$) with different symbols for each group and each axis. The magnetization of the $IRM_{0.1T}$ axis represents 50 to 67% of the total IRM at room temperature. It demagnetizes rapidly along a linear or concave decay curve typical of titanomagnetite and with full removal between 550°C and 600°C corresponding to the Curie temperature of magnetite (maximum $IRM_{0.1T@600°C}/IRM_{@20°C}$ at 1.5%). No significant change is observed in the decay rate of this component around 300-350°C (red triangles in Fig. 6a-c). This information together with relatively low and constant IRM_{1T}/κ ratio (around 10 kA/m; Table 3) suggests that sulfides do not contribute a significant amount to the ferrimagnetic signature of the samples (Snowball and Thompson, 1990; Peters and Dekkers, 2003).

In all cases, the high coercivity component (IRM_{1T}) is the weakest magnetization and its contribution to the total $IRM_{@20°C}$ varies between 2 and 22% (Fig. 6). No significant decrease is observed through the first 5 demagnetization steps between room temperature and 120°C, the characteristic Néel temperature of goethite (Özdemir and Dunlop, 1996). On the contrary, the decay rate is monotonous until high temperatures (Fig. 6a-c). Goethite has been recognized by DRS technique in the southern basin (Zhang et al., 2007) so we cannot exclude its contribution to the high coercivity mineralogical cortege, but it is not at the level of the hematite contribution. The magnetization of IRM_{1T} is fully removed at temperatures sometimes coinciding with that of the $IRM_{0.1T}$ axis (Fig. 6c), sometimes between 650°C and 700°C, the Néel temperature of hematite (Fig. 6a-b).

The $IRM_{0.3T}$ component is clearly an intermediate between the other two. It carries 26 to 41% to the total IRM and the fraction remaining after heating at 600°C ($IRM_{0.3T@600°C}/IRM_{@20°C}$) ranges between 0.05 and 2.5% of the initial total IRM.

These results illustrate variable magnetite/hematite content and when the percentage of IRM remaining at 600°C on this 1T component ($IRM_{1T@600°C}/IRM_{@20°C}$) is reported versus age, it is clearly anticorrelated to the S-ratio in each core (Fig. 5). The lowest S-ratio values are therefore directly associated to the highest proportion of hematite, confirming that changes in the S-ratio illustrate variable amounts of magnetite and hematite, excluding significant contributions of other minerals such as goethite and iron sulfides.

5.3 Magnetic grain sizes

Although hematite is often present as described above, the low coercivity minerals dominate the magnetic signal. Therefore the ARM/κ and ARM/IRM ratios can be used as magnetic grain size proxies (Figure 7). In all cases, both ratios yield the same variations. The records are rather similar among cores from the southern and central regions and, except for the Toba ash layer which is obviously constituted of relatively coarse magnetic minerals (Fig.

7b-c) both ratios vary by a factor of 2 to 3 (Fig. 7a to e). In the northern group, the ARM/κ ratio varies by a factor of about 6 and the ARM/IRM ratio by a factor of 3 to 4 (Fig. 7f-g). The two northern cores also have very similar magnetic grain size profiles but different from those of the other cores.

When the hysteresis parameters are reported on a Day diagram (Day et al., 1977) revised by Dunlop (2002), the data points are distributed between the theoretical superparamagnetic - single-domain (SP-SD) and the single-domain - multidomain (SD-MD) mixing lines (Fig. 8). The relationship with the SP-SD mixing line is unclear. Indeed, superparamagnetism has a significant impact on κ. Except if it is constant in all cores which is very unlikely, it should therefore distort the ARM/κ ratio with respect to the ARM/IRM one and this is not observed. Therefore, the distribution of the points seems more related to the SD-MD mixing line and indicates 30 to 60% of MD in the central and southern groups and 65 to 85% of MD in the northern group (Fig. 8).

We may wonder whether the magnetite grain sizes in the center and the south, finer on the average than in the north, are due to the presence of SD biogenic magnetites in the south. Indeed, more and more studies suggest that biogenic magnetites are ubiquitous in the ocean (Yamazaki and Ikehara, 2012, Channell et al., 2013; Ouyang et al. 2014b). However, the question of their real presence and of their contribution to the total magnetic signal in the SCS is still open.

In core 86 GC from the southern basin of the SCS, Ouyang et al. (2014a) concluded that magnetite was only of detrital origin with no contribution from biogenic magnetite. In the central basin, however, a medium coercivity component and the central ridge in the high resolution FORC diagram suggested the presence of biogenic magnetite (core PC24; Ouyang et al., 2014b; 2016) while in another core (PC338; Li et al., 2018) the medium coercivity component is attributed to magnetite inclusions in silicate minerals. In the latter case, the authors interpret the co-variation of the medium-coercivity component with the detrital-type magnetite as a control of both components by weathering processes rather than biogenic ones. This contribution of possible biogenic magnetite was discussed again by Kissel et al. (2018). In a core-top sample from the northern basin characterized by a rather significant medium coercivity component, these authors quantified the contribution of the central ridge in the FORC diagram to only 2% of the saturation of the low coercivity remanence.

In the center and southern part, FORC diagrams are more difficult to obtain than in the north due to the low level of magnetization which increases the noise level. Therefore, in order to address this question in the cores we examine here, we decomposed IRM acquisition curves into cumulative log-Gaussian components (CLG) using the software delivered by Kruiver et al. (2001). In all our cores, the best fit characterized by the minimum sum of squared residuals is obtained with four components. Examples from the two most contrasted areas (southern core MD01-2393 and northern ODP site 1145) and time period during which fine grains are observed (~125 ka) are shown in Figure 9a,f. The downcore variations of the different parameters characterizing the CLG components (contribution, B1/2 and DP, see Table 2) are shown in Figure 9c-e for ODP site 1145 and in Figure 9g-j for core MD01-2393. The magnetic grain size as reconstructed by the ARM/IRM ratio is given for comparison in Figure 9 b,g. The first component (CLG1) with the lowest B1/2 (~ 5 mT) contributes for less than 10 % to the total IRM and it is poorly defined with a large dispersion parameter (DP up to 0.8 mT). It corresponds to the first points of the IRM acquisition curve and represents the very low coercivity tail. In the north, the two main components contributing to the IRM are CLG2 and CLG3 (~ 55 and 30% on the average, respectively) because the high coercivity CLG4 is largely minor and even difficult to quantify (<10%) (Fig. 9c). The median acquisition fields B1/2 for CLG2 and CLG3 are on the average about 30 and 65 mT, respectively, with DP about 0.4 and 0.2 mT, respectively (Fig. 9d,e).

In the southern cores, the contribution of the high coercivity CLG4 (B1/2 ~ 1T) to the total IRM ranges from 10 to 33%. On the average, CLG3 contributes similarly with the same B1/2 and DP than in the north (Fig.9 h-j). However, we observe that its contribution along the core (23 to 38 %) co-varies with that of CLG2 component and both are in opposite to the contribution of high coercivity component CLG4. (Fig. 9h). This is the duality between magnetite and hematite mentioned above and already observed in the S-ratio. The observed southward fining of the magnetic fraction is illustrated on the average by the higher B1/2 of CLG2 (~40 mT) and its co-variability with CLG3.

In summary, two soft components are always observed in the magnetite fraction and they largely overlap in coercivity (Fig. 9a,f). If the association of CLG2 with detrital magnetite is largely accepted, the full attribution of CLG3 to biogenic magnetite is still discussed (Kissel et al., 2018). In the north, both are uniformly distributed down core. In the south, CLG2 contributes less than in the north and it is harder. Together with its co-variation with CLG3 it may explain the general fining of the southern cores with respect to the northern ones. In addition, the variations in magnetite grain sizes as shown by ARM/IRM ratio is also recorded in the hard/softness (B1/2) of the detrital component CLG3. The coercivity changes of CLG2 and the co-variations of the contributions of CLG2 and CLG3, in opposite to that of CLG4 suggest that both low coercivity components are in the detrital part. In the example treated by Kissel et al. (2018), the contribution of the CLG3 component was significantly higher than the one we have here. However, the "real" biogenic component was very weakly contributing. Therefore, waiting for results from still underway investigations, we think that the largest contribution to the magnetic signal we observe is due to detrital magnetites and that biogenic magnetite does not play the main role in the fining of the magnetic fraction.

6. Discussion

The two main variable characteristics of the sedimentary magnetic fraction in the SCS, which account for the changes in all the parameters we measured, are the magnetite grain size and magnetic mineralogy. Both ARM/κ and ARM/IRM ratios yield similar answer in each core and we chose the ARM/IRM ratio to illustrate the magnetic grain (Table 2). The magnetic mineralogy varies in first approximation between different proportions of magnetite and hematite and we showed that S-ratio is the appropriate and sensitive parameter to describe it continuously along the cores.

6.1 Space and time distribution of magnetic mineralogy and grain size

Detrital magnetite is present in all cores and its grain size is finer on the average in the southern and central regions (average ARM/IRM ratio around 10^{-1}) than in the north (~3 to 4 x 10^{-2}) (Fig. 10) as confirmed by the distribution of the hysteresis parameters on the Day/Dunlop diagram (Fig. 8). The two northern cores are rather deep but, as shown in Fig. 6a, their magnetic grain size is similar to that observed in the nearby shallower (2125 m) core MD12-3432 (Chen et al., 2017b). Therefore, in each region, the average magnetic grain size does not depend on the water depth of the cores on the slope and the deep basin and the observed differences are inter-regional. This confirms the observation already made on core-tops (Kissel et al., 2018).

In the northern cores a coarser event is observed at the beginning of MIS3 between 60 and 40 kyr (Fig. 5), consistent with the low values observed in other parameters (Fig. 4). This event could result from diagenetic processes at the inception of MIS3 which would have ended in the middle of MIS3 but because it was not observed elsewhere, it needs to be further scrutinized before reaching any robust interpretation. We do not have any clear interpretation for this event at present. Except for this event, the grain size of magnetite is rather uniform over the last climatic cycle. On the contrary, in the central and southern cores, the magnetite grain size fluctuates continuously and it is systematically coarser during glacial periods compared to interglacial ones. These variations account for the distribution also observed in the Day/Dunlop diagram between 30 to 60% of MD (Fig. 6a) and in the coercivity changes of CLG2 (Fig. 9j). In case CLG3 would, at least partly, correspond to biogenic magnetite, it does not control the observed pattern because it is not higher during interglacials compared to glacials.

Together with magnetite, variable amounts of hematite are present in the cores. When the S-ratios are all reported on the same scale, three different groups of curves are clearly identified (Fig. 10) and they correspond to the three studied geographical areas. For the northern group, the S-ratio, on the average about 0.95, is consistent with the dominance of magnetite. It decreases in the central group (about 0.86) and even more in the southern group (about 0.81) (Table 3). The distribution of the S-ratio therefore indicates a significant southward increase in hematite. Although in these cores, magnetite still dominates the magnetic signal due to the very weak characteristic magnetization of hematite, the latter is very abundant in volume. It may indeed represent as much as 90 wt% in the sedimentary magnetic fraction for a S-ratio of 0.8 (Frank and Nowaczyk, 2008).

The magnetic mineralogy also varies differently in time, depending on the region. Indeed, the amplitude of the fluctuations of the S-ratio increases southward reaching the maximum (from 0.7 to 0.9) in core MD01-2393 from the southern group while it varies from 0.83 to 0.93 at most in the center and from 0.9 to 0.98 in the northern group. The small-scale amplitude variations in the north do not seem to be related to orbital scale climatic changes as illustrated by the benthic oxygen isotope stack LR04. On the contrary, the time fluctuations of the S-ratio in the center and the south are climatically-driven with maxima during Holocene and substage 5e and minima during the LGM and MIS4 and 6 (except for the Toba ash defined by an S-ratio close to 1 in cores MD01-2393 and ODP1143). The other periods are characterized by intermediate values with also some variability, in particular during MIS5. In the southern ODP core 1143, if goethite contributes to the low S-ratio value, its abundance is not driven by glacial/interglacial cycles (Zhang et al., 2007), so that hematite remains the main magnetic mineral to examine. We observe that the differences between the S-ratio curves of the three groups increase significantly during glacial periods.

The composition of the detrital magnetic fraction deposited at each site in the SCS is therefore variable both geographically from north to south and in time from MIS6 to the Holocene. These variations might result from changes in the composition of the source, in the provenance area, in the transport path from a given source and/or in the transport efficiency.

6.2 Provenance of the sediment

The study of the river sediments evidenced present-day regional differences in the composition of the riverborne magnetic fraction. These differences mainly reflect the nature of the parent-rocks. A southward enrichment of the river sediments in hematite is illustrated by the magnetic composition of the sediments from the Mekong, the Malay Peninsula, western and northwestern Borneo compared to the one from Pearl River, Luzon and Taiwan (Kissel et al., 2016; 2017). The Red River has a magnetic composition intermediate between these two groups (Kissel et al., 2016). Some scatter is observed in the magnetite grain sizes delivered by each river system but on the average, they are relatively coarse (ARM/IRM around 1 to 2 x 10^{-2}) and not geographically-dependent. The hysteresis parameters correspond to 60 to 90% of MD grains (M_{rs}/M_s – H_{cr}/H_c ratios from 0.18 – 2.47 to 0.06 – 5.46) (Fig. 6b).

The magnetic properties of the marine cores reflect those of modern river sediments in variable ways. The magnetite grain size in the northern cores is similar to that of the river samples (Fig. 6) while it is finer on the average in the cores from the center and southern groups. We have seen that biogenic magnetite does not account significantly for finer magnetic fraction in the central and southern group. Because the coarsest part of the sediment is trapped on the shelves (Liu et al., 2010; Y. Zhong et al., 2017) and close to the river mouths, the distribution of the fine grains along the slope and in the deep basin depends on the distance to the source and on the transport dynamic. This will be discussed below.

The magnetic mineralogical composition of the marine sediments can be compared to that of river samples and this is shown in Figure 11 where the mean S-ratio values and their 1σ dispersion are reported for each fluvial system together with the S-ratio of the paleorecords. The north-south gradient in the mean S-ratio from marine cores indicates various provenance areas for the sediments.

Magnetite which characterizes the magnetic fraction in the northern cores is not geographically discriminant in terms of provenance because Luzon, Taiwan and the Pearl River contribute all to its delivery to the sea. Based on clay and major element content, Taiwan and Luzon are described as the modern main terrigenous contributors to the sediment deposited in this area (Liu et al., 2016 and references therein). The Pearl River sediments, at least for the clay fraction, would be transported southwestward before settling down on the continental platform. However, Yang et al. (2016) recognized the Pearl river signature in sediments collected at about 1100 m water depth, south of the Pearl river mouth and Liu et al. (2013) noticed that Pearl River sediments also presently reach areas as south as and as deep as the Xisha trough. So we cannot exclude that the Pearl River also participates to the magnetic fraction of our cores.

In the central region, the mean S-ratio value, lower than that of the northern cores, is close to the one measured in the Red River sediments. This is therefore the closest river catchment contributing to the detrital input to our sites. This is consistent with the clay and REE composition from a nearby surface sediments (Liu et al., 2013) and the composition of sediments collected at 1500 m in a trap located in the Xisha trough where 20 to 50% of the sediment is attributed to the Red River (Liu J. et al., 2014). However, if the Red River source is well recognized in this area the contribution of the Pearl River versus Taiwan is still debated at present (Liu et al., 2013; 2016; Li et al., 2018).

The large amplitude variations in the S-ratio of the southern cores are in the same range as those observed in the Mekong and in rivers from Kalimantan and eastern Malay Peninsula. Part of the fluvial sediments from Kalimantan are most likely trapped in the Northwest Borneo trough (Hutchison, 2010) but it has been shown that they also presently reach the deep southern basin (Liu et al., 2013).

As an average, the comparison between the S-ratio obtained from land and from deep sea cores allows to identify the main continental sources of the magnetic particles in each basin. Indeed, the magnetic mineralogical composition of marine sediments reflects on the average the composition of the sediment from the closest rivers. However, significant time variations are superimposed to these average values, at least in the central and southern basins. They illustrate variable mineralogical mixtures in time, most likely related to both changes in the sea level changes and in the oceanic circulation.

6.3 Magnetic signature of sea level changes and oceanic circulation

While the magnetic composition of the sediments in the northern basin remained rather uniform over the last climatic cycle, this is not the case for the central and southern groups.

In the northern basin, the sedimentation rate increases during glacial time, in particular during MIS4 (Fig. S1). This was already observed by Chen et al. (2017b) in core MD12-3432 for older glacial periods (MIS10, 8 and 6). It is interesting to note that in both cases, the maximum of sedimentation rate occurs preferentially at the end of the glacial period, maybe illustrating the progressive increasing erosional capacity of the rivers extended on the newly emerged lands. However, by contrast with the results of Chen et al. (2017b) describing coarser magnetite grains during glacials, magnetite with uniform grain size characterizes the last climatic cycle in our cores and no change is observed with sea-level variations (Fig. 9, 10). At ODP site 1146, Kissel et al. (2003) already noticed that the relationship between magnetic properties and glacial/interglacial variability changed around marine isotopic stage 6 and this maybe due to changes in the geometry of the continental slope as suggested by Sun et al. (2003).

Because of the uniformity of the magnetic content in our northern cores, the bulk magnetic parameters κ; ARM and IRM can be interpreted as concentration-dependent parameters (except between 60 and 40 kyr corresponding to a coarse grain event). As shown in Figure 4, the increase in these parameters at the two terminations illustrates more magnetite particles during MIS5 and Holocene than during full glacial periods. If magnetite in this region, similarly to clay minerals, essentially originates from Luzon and Taiwan (Liu et al., 2013; 2016), sea level rise cannot account for the observed changes due to the absence of continental platform off these two islands. Increased precipitations on land also unlikely account for these changes in magnetite concentration because they are not related to any precessional periodicity which controls the rain season. Finally, the observed variations may result from a strengthening of bottom current in the northern part of the SCS during interglacials compared to glacials.

In the central and southern basins, by contrast with the northern group, the magnetic composition of the sediment is clearly sensitive to global climatic changes. Relatively coarser magnetite grains are deposited together with higher hematite content during glacial periods compared to interglacial ones. We observe here a combined effect of sea level and oceanic circulation changes.

According to previous observations that magnetic grain sizes vary similarly to the physical grain size (Kissel et al., 2013 in North Atlantic, Hu et al., 2012 and Chen et al., 2017b in the SCS), the slightly coarser nature of the magnetic particles during glacial time can be attributed to the more incisive character of the rivers on the shelves, re-suspending and transporting to the continental slope and the deep basin sediments previously deposited on the shelves during interglacial periods.

During glacial times, when the sea level decreases, the sediment transported to the continental slope originates both from the continental catchment and from the shelf where it has been previously deposited and from which it is newly eroded. The fact that the glacial magnetic composition of marine sediments is close to the modern composition on land indicates that the different interglacial/glacial climatic conditions did not significantly affect the magnetic mineralogy delivered at sea. Off the Pearl river hematite supply has been considered as resulting from enhanced oxidation processes during cold periods (Hu et al., 2012). However, nowadays, the magnetic composition of the river sediments on land is known and indicates that hematite is already significantly abundant at present in the Red River and also in the Mekong basin and in Kalimantan, the main regions feeding the southern part of the SCS. Therefore, although we cannot exclude that part of hematite is also formed on the emerged shelf under dry climate, the results suggest that it is a stable tracer in time of the southern continental regions. This is consistent with the observation that chemical weathering is very weak in the Mekong basin over the last 30 kyr (i.e. over glacial to Holocene period) (Jiwarungrueangkul et al., 2019). Consequently, the differences between glacial and interglacial magnetic sedimentary composition in the SCS result from changes in the transport pathway and efficiency rather than in the composition of the source area. This is an important source of information about paleoenvironmental changes in this area. Indeed, for other proxies such as clays, it is usually the other way around: their modern composition at sea is close to the modern continental one and past changes are interpreted as changes in the physical alteration/chemical weathering context on land (Steinke et al., 2008; Liu et al., 2016), sometimes difficult to separate from effects of sea level or oceanic circulation changes.

The important additional information yielded by our results is that the interglacial (including Holocene) composition of the magnetic fraction only partially reflects the one of the sediments delivered by the closest rivers at present. Indeed, the attenuation of the north-south contrast in the magnetite versus hematite content mentioned in core-tops compared to river samples (Kissel et al., 2018) is now also observed for the entire Holocene and for MIS5. As mentioned above, hematite is a very sensitive tracer due to its weak magnetization easily surpassed by that of magnetite. Our results show that in the central and southern basins, whilst the glacial marine magnetic mineralogy is rather "pure" in terms of hematite content of the present-day close-by continental composition, it indicates a mixture of provenances during interglacials.

The magnetic properties described above indicate that magnetite is mainly of detrital origin. The fraction sourcing from Sumatra (Kissel et al., 2017) very unlikely reached the deep southern SCS basin during interglacial periods given the size of the Sunda shelf. We would rather expect it to be delivered to the deep basin during low sea level periods when the Molengraaff river was functioning (Voris, 2000). However, this is not the case as magnetite content does not increase during low sea level periods. So the interglacial distribution of detrital magnetite within the SCS may be controlled by the oceanic circulation. Magnetite concentration is indeed presently about one order of magnitude larger in the north than in the south. The fine-grain magnetite deposited in the center and southern regions during high sea level periods is likely at least partly transported from the north. This transport may work by deposition/suspension cycles under the influence of the strong winter coastal current at the surface and on the shelf and/or by the cyclonic gyres at depth. The geographical difference in the average magnetite grain size between the northern basin on one side and central and southern basins on the other side might also result from this oceanic transport due to differences in transport distances from the source area. This is consistent with the various observations around the Xisha islands that sediments from Taiwan and the Pearl river are presently transported by bottom current as far south as at least these areas (Yang et al., 2016; Liu et al., 2013). It is also consistent with the observation that the magnetite content is more efficiently transported from Luzon and Taiwan to the sites from the northern group during interglacials than during glacials.

Our results obtained along a north-south transect suggest a weaker deep-sea circulation during glacial times compared to interglacials. It is a novel interpretation of the magnetic properties of deep-sea sediments in the SCS. Indeed, as mentioned above, the magnetic analyses previously performed on cores located on the northern continental slope concluded about a stronger bottom current during cold and dry periods, in particular short climatic events such as Heinrich event, Younger Dryas (Fig. 2). These conclusions were based on increased magnetic and/or sediment grain size and on increased degree of magnetic anisotropy (Zheng et al., 2016; Li et al., 2019). Indeed, the anisotropy of the low field magnetic susceptibility would be the perfect method to reconstruct such changes in the bottom current strength. However, as already discussed in section 3, the anisotropy results are difficult to interpret in hemipelagic clay-rich sediments containing variable magnetic mineralogy. It is also difficult to decipher the role of bottom current strength and sea-level variations by coupling magnetic or sedimentary grain sizes in highly detrital-rich environments, close to land sources. The magnetic mineralogy based on the detailed knowledge of the provenance area is therefore of unique potential in this kind of study.

Our conclusions about a weaker deep-sea circulation in the SCS during glacial periods compared to interglacials are consistent with the differences in radiocarbon ages between planktonic and benthic foraminifera reported by Wan and Jian (2014) in the northern and in the southern basins over the last 35 ka. A strong southward advection from the Luzon strait together with strong vertical mixing is suggested to explain the younger ventilation ages observed by the authors in the southern basin compared to the northern one during the Holocene. During the last glacial, the gradient between southern and northern basins was reversed and southern waters were older than the northern ones, illustrating a weak intrabasin exchange and a weak deep water ventilation most likely related to reduced mixing and limited advection (Wan and Jian, 2014). This conclusion was recently confirmed on the basis of benthic $\delta^{18}O$ and $\delta^{13}C$ depth profiles which revealed an enhanced bathyal density stratification on the SCS during the glacial period with respect to the Holocene (Wan et al., 2018).

6.4 Long-term oceanic circulation changes

The alternation in the southern basin of magnetite-rich and hematite-rich periods is confirmed over the last 900 ka (Fig. 12b) while, over the same time period, magnetite remains the main magnetic component in the north (Fig. 12c). The ΔS-ratio calculated as the difference between the northern and the southern S-ratio is also reported in Figure 12d. As for the last climatic cycle, we interpret this difference as resulting from a glacial/interglacial interplay of changes in sea level and deep-sea current dynamic with low values illustrating mixed magnetic mineralogy from different sources around the SCS and transported by various water masses and high values illustrating more “pure” nearby river signatures resulting from low sea level and weak deep-sea basin-scale circulation. This process is therefore periodically repeated over the last 1 Ma.

Superimposed to this strong glacial-interglacial cyclicity, the ΔS-ratio curve can be fitted on the long-term, by a polynomial curve culminating around 500 ka (Fig. 12d). Following the interpretation given above for the 100 kyr cycle, this suggests a maximum southward advection of deep-waters from the Luzon strait and therefore active deep-sea circulation during the mid-Brunhes event (MIS 13). This record is too short to allow any robust identification of long-term cyclicity. However, its pattern is similar to that of numerous longer records in which 500 kyr climatic periodicity is recognized over the last 1.6 Ma in particular with the benthic $\delta^{13}C$ maximum at 500 kyr (e.g. Wang et al., 2014). The latter is presently confirmed by a new record obtained from the deep western equatorial Pacific, at a site bathed by the low circumpolar deep water (Dang et al., 2020). As seen in Figure 12e, the similarity between this new record and our ΔS-ratio curve is remarkable both on the glacial/interglacial scale and on the longer-term. The maximum magnetic mineralogical mixing in the SCS (ΔS-ratio ~ 0) coincides with the maximum invasion of the western equatorial Pacific by southern-sourced waters. Also, the ΔS-ratio curve is extremely similar to that of the coarse fraction index proposed by Bassinot et al. (1994) as a tracer for calcium carbonate dissolution (Fig. 12f). The latter, based on two marine sequences from the Arabian sea and the equatorial Indian ocean illustrates the variable impact of southern-source corrosive waters with time. The high carbonate dissolution, the benthic $\delta^{13}C$ maximum and the minimum in the SCS ΔS-ratio indicate that changes in the deep SCS mixing and circulation are largely related to global deep circulation changes and global carbon cycle.

7. Conclusions and summary

After examining how various magnetic properties of deep-sea sediments from the SCS are interpreted in the different studies conducted so far, we take advantage of the recent magnetic characterization of river borne sediments to interpret and discuss magnetic results obtained from cores distributed along a N-S transect and divided in three groups (north, center and south) for the description of the results. The following observations could be made:

- Magnetic properties do not depend on the water depth at which the cores have been collected in each of the studied group of cores between about 1500 and 3400 m.
- Magnetic grain size and mineralogy show time and space variability.
- In a general way, over the last climatic cycle, magnetite grains are coarser in the northern part than in the central and the southern parts of the SCS.

- Magnetic grain size is uniform in the northern sites while it fluctuates in the central and southern basins.

- Northern cores are characterized by magnetite while central and southern cores contain variable amounts of hematite at the glacial/interglacial scale.

- The magnetic mineralogical composition of marine sediments in the central and southern groups is closer to the one of the nearby fluvial source during glacial than during interglacial periods while it is mixed with another source during interglacials.

This led us to draw the following conclusions about the interplay of sea level changes and bottom oceanic circulation:

- In the central and southern basin, local fluctuations in magnetite grain sizes most likely result from sea level changes.

- Increased amounts of magnetite at the northern sites during interglacial reflects enhanced bottom current transporting magnetite mainly from Taiwan and Luzon with probably a small contribution from the Pearl River.

- In the central and southern group, the interglacial enrichment in magnetite with respect to the river-borne sediment most likely results from a southward transport of the northern sourced particles, consistently with the fact that they are in average finer than in the north.

- The more "pure" fluvial magnetic composition observed in the central and southern group during glacial suggests a less active bottom circulation, consistently with results about the aging and low ventilation of deep-water masses in the southern part of the SCS.

- The magnetic mineralogy variability pattern observed at 100 kyr pacing is recorded over the last 900 ka.

- On the long-term, superimposed to this 100 kyr cycle, mineralogical mixing by deep-sea active advection increases between 900 kyr and 500 kyr and then decreases. The culmination around 500 ka is in phase with carbonate dissolution and benthic $\delta^{13}C$ maximum observed in many regions around the world. This maximum illustrates a more active invasion of southern-sourced waters indicating that the deep oceanic circulation in the SCS is closely related to global oceanic circulation changes.

Acknowledgments

We are grateful to the crew of the R.V. *Marion Dufresne* (IPEV) cruise who allowed us to collect such nice cores during the Marco Polo 1. This research used also samples provided by the Ocean Drilling Program (ODP). This study has been conducted in the framework of the Laboratoire International Associé MONOCL (Monsoon, Ocean and Climate). We are grateful to Haowen Dang and Franck Bassinot for sharing their numerical data. MRV acknowledges a post-doctoral grant, G-25338-T, from Conacyt and support from CNRS France for a post-doctoral position at LSCE. Two anonymous referees helped us in improving and clarify the manuscript. Financial support for the magnetic analyses performed at LSCE was provided by the national French inter-institutes program LEFE (MONOCL project), by the Centre National de la Recherche Scientifique, by the French Commissariat à l'Energie Atomique et aux Energies Alternatives. ZJ acknowledges a research grant (No. 2018YFE0202400) from the Ministry of Science and Technology of China. This is LSCE contribution XXX.

References

Abdullah, N.T., 2009. Mesozoic stratigraphy, in: Hutchison, C.S., Tan, D.N.K. (Eds.), Geology of Peninsular Malaysia. University of Malaya/Geological Society of Malaysia, Kuala Lumpur, pp. 87-132 (449 pp., Chapter 6).

Abdullahi, M.G., Toriman, M.E., Gazim, M.B., Juahir, H., 2014. Rainfall dynamics of Terengganu, Malaysia and its recent trends analysis using MannKendall test. J. Adv. Biotechnol. 4 (2), 372-381.

Bachman, S.B., Lewis, S.D., Schweller,W.J., 1983. Evolution of a Forearc Basin, Luzon Central Valley, Philippines. Am. Assoc. Petrol. Geol. Bull. 67, 1143-1162.

Banerjee, S.K., King, J. and Marvin, J. 1981. A rapid method for magnetic granulometry with applications to environmental studies, Geophys. Res. Lett. 8, 333-336. https://doi.org/10.1029/GL008i004p00333

Barber, A.J., Crow, M.J., 2009. Structure of Sumatra and its implications for the tectonic assembly of Southeast Asia and the destruction of Paleotethys. Island Arc 18, 3-20. https://doi.org/10.1111/j.1440-1738.2008.00631.x

Bassinot, F.C., Beaufort, L., Vincent, E., Labeyrie, L., Rostek, F., Müller, P.J., Quidelleur, X., Lancelot, Y., 1994. Coarse fraction fluctuations in pelagic carbonate sediments from the tropical Indian Ocean: a 1500-kyr record of carbonate dissolution. Paleoceanogr. 9, 579-600.

Bassinot, F., and Baltzer, A., 2002. WEPAMA, MD122 IMAGES VII cruise report, IPEV. In Les rapports des campagnes à la mer, ISSN [1636–8525], 2002, 01.

Bindoff, N.L., P.A. Stott, K.M. AchutaRao, M.R. Allen, N. Gillett, D. Gutzler, K. Hansingo, G. Hegerl, Y. Hu, S. Jain, I.I. Mokhov, J. Overland, J. Perlwitz, R. Sebbari and X. Zhang, 2013: Detection and Attribution of Climate Change: from Global to Regional, in: Stocker, T.F., D. Qin, G.K. Plattner, M. Tignor, S.K. Allen, J. Boschung, A. Nauels, Y. Xia, V. Bex and P.M. Midgley (eds.), Climate Change 2013: The Physical Science Basis. Contribution of Working Group I to the Fifth Assessment Report of the Intergovernmental Panel on Climate Change. Cambridge University Press, Cambridge, United Kingdom and New York, NY, USA.

Bühring, C., Sarnthein, M., Leg 184 Shipboard Party, 2000. Toba ash layers in the South China Sea: Evidence of contrasting wind directions during eruption ca. 74 ka. Geology, 28(3) 275–278.

Cecil, C. B., Dulong, F. T., Harris, R. A., Cobb, J. C., Gluskoter, H. G., Nugroho, H., (2003) Observations on climate and sediment discharge in selected tropical rivers, Indonesia, in: C. B. Cecil and N. T. Edgar (Eds), Climate Controls on Stratigraphy, SEPM (Society for Sedimentary Geology), Special Publication 77, ISBN 1565760859, 29–50.

Chang, Y.T., Hsu, W.L., Tai, J.H., Tang, T., Chang, M. H., Chao, S.Y., 2010. Cold deep water in the South China Sea, J. Oceanogr. 66(2), 183-190.

Chen, C. T. A., Huang, M. H., 1996. A mid-depth front separating the South China Sea Water and the Philippine Sea Water. J. Oceanogr., 52, 17-25.

Chen, C. T. A., Wang, S., Wang, B., Pai, S. C., 2001. Nutrients budgets for the South China Sea basin. Mar. Chem., 75, 281–300.

Chen, H., Xie, X.N., Zhang, W.Y., Shu, Y.Q., Wang, D.X., Vandorpe, T., Rooij, D.V., 2016. Deepwater sedimentary systems and their relationship with bottom currents at the intersection of Xisha Trough and Northwest SubBasin, South China Sea. Mar. Geol. 378, 101–113. https://doi.org/10.1016/j.margeo.2015.11.002.

Chen, Z., Yan, W., Tan, X., Liu, J., Chen, M., Yang, H., 2009. Magnetic susceptibility in surface sediments in the southern South China Sea and its implication for subsea methane venting. J. Earth Sci. 20, 193–204. https://doi.org/10.1007/s125830090019y.

Chen, Q., Liu, Z., Kissel, C., 2017a. Clay mineralogical and geochemical proxies of the East Asian summer monsoon evolution in the South China Sea during Late Quaternary. Sci. Rep. 7, 42083; doi: 10.1038/srep42083

Chen, Q., Kissel, C., Liu, Z., 2017b. Late Quaternary climatic forcing on the terrigenous supply in the northern South China Sea during Late Quaternary: input from magnetic studies. Earth Planet. Sci. Lett. 471, 160-171. http://dx.doi.org/10.1016/j.epsl.2017.04.047.

Clemens, S.C., Prell, W., Murray, D., Shimmield, G., Weedon, G., 1991. Forcing mechanisms of the Indian Ocean monsoon. Nature 353, 720-725.

Clemens, S.C., Prell, W.L., 2007. The timing of orbital scale Indian monsoon changes. Quat. Sci. Rev. 26, 275–278. https://doi.org/10.1016/j.quascirev.2006.11.010.

Clemens, S.C., Prell, W.L., Sun, Y., 2010. Orbital scale timing and mechanisms driving Late Pleistocene IndoAsian summer monsoons: reinterpreting cave speleothem δ18O. Paleoceanogr. 25, PA4207. http://dx.doi.org/10.1029/2010PA001926.

Clift, P.D. 2015. Assessing effective provenance methods for fluvial sediment in the South China Sea, in: Clift, P.D., Harff, J., Wu, J. & Qui, Y. (eds) River Dominated Shelf Sediments of East Asian Seas. Geological Society, London, Special Publications, 429. First published online September 3, 2015, updated May 26, 2016, http://doi.org/10.1144/SP429.3

Dang, H., Peng, M., Ma, X., Wan, S., Jian, Z., 2020. Possible linkage between the long-eccentricity marine carbon cycle and the deep-Pacific circulation: Western equatorial Pacific benthic foraminifera evidences of the last 4Ma. Mar. Micropal., 155, https://doi.org/10.1016/j.marmicro.2019.101797.

Day, R., Fuller, M., Schmidt, V.A., 1977. Hysteresis properties of titano-magnetite: grain-size and compositional dependence. Phys. Earth Planet. Inter. 13, 260–267.

Dippner J, Nguyen K, Hein H, Ohde T, Loick N. 2007. Monsoon induced upwelling off the Vietnamese coast. Ocean Dynamics 57(1), 46-62. https://doi.org/10.1007/s10236-006-0091-0

Dong, L., Li, L., Li, Q., Wang, H., Zhang, C. L., 2015. Hydroclimate implications of thermocline variability in the southern South China Sea over the past 180,000 yr, Quat. Res., 83 (2) 370-377.

Dung, B.V., Stattegger, K., Unverricht, D., Phach, P.V., Thanh, N.T., 2013. Late Pleistocene–Holocene seismic stratigraphy of the Southeast Vietnam Shelf. Global Planet. Change 110, 156-169.

Dunlop, D. J., 2002. Theory and application of the Day plot (Mrs/Ms versus Hcr/Hc) 1. Theoretical curves and tests using titanomagnetite data. J. Geophys. Res. 107(B3), 2056. https://doi.org/10.1029/2001JB000486.

Egli, R. (2004). Characterization of individual rock magnetic components by analysis of remanence curves. 3. Bacterial magnetite and natural processes in lakes. Physics and Chemistry of the Earth, 29(13-14), 869–884. https://doi.org/10.1016/j.pce.2004.03.010

Frank, U., Nowaczyk, N.R., 2008. Mineral magnetic properties of artificial samples systematically mixed from haematite and magnetite. Geophys. J. Int. 175, 449-461.

Gan, J., Liu, Z., Hui, C.R., 2016. A Three Layer Alternating Spinning Circulation in the South China Sea, J. Phys. Oceano. 46, 23092315.

Gupta, A., 2009. Geology and landforms of the Mekong Basin. In: The Mekong. I.C. Campbell, Ed., Academic Press, San Diego. Pp 29-51.

Hanebuth, T. J.J., Voris, H. K., Yokoyama, Y., Saito, Y., Okuno, J., 2011. Formation and fate of sedimentary depocentres on Southeast Asia's Sunda Shelf over the past sea level cycle and biogeographic implications, Earth Sci. Rev. 104, 92-110, https://doi.org/10.1016/j.earscirev.2010.09.006.

He, Q., Zhan, H., Cai, S., He, Y., Huang, G., Zhan, W., 2018. A new assessment of mesoscale eddies in the South China Sea: Surface features, threedimensional structures, and thermohaline transports. J. Geophys. Res. Oceans, 123. https://doi.org/10.1029/2018JC014054.

Hiscott, R.N., 2001. Depositional sequences controlled by high rates of sediment supply, sealevel variations, and growth faulting: the Quaternary Baram Delta of northwestern Borneo. Mar. Geol. 175, 67-102.

Horng, C.S., Huh, C.A., 2011. Magnetic properties as tracers for sourcetosink dispersal of sediments: a case study in the Taiwan strait. Earth Planet. Sci. Lett. 309, 141-152.

Horng, C.S., Huh, C.A., Chen, K.H., Lin, C.H., Shea, K.S., Hsiung, K.H., 2012. Pyrrhotite as a tracer for denudation of the Taiwan orogen. Geochem. Geophys. Geosyst. 13: Q08Z47. https://doi.org/10.1029/2012GC004195.

Hu, J., Kawamura, H., Hong, H., Qi, Y., 2000. A Review on the Currents in the South China Sea: Seasonal Circulation, South China Sea Warm Current and Kuroshio Intrusion. J. Oceanogr. 56, 607624.

Hu, D., Böning, P., Köhler, C.M., Hillier, S., Pressling, N., Wan, S., Brumsack, H. J., Clift, P.D., 2012. Deep sea records of the continental weathering and erosion response to East Asian monsoon intensification since 14 ka in the South China Sea, Chem. Geol., 326327, 118 ; https://doi.org/10.1016/j.chemgeo.2012.07.024.

Huang, E., Tian, J., 2012. Sea level rises at Heinrich stadials of early Marine Isotope Stage 3: evidence of terrigenous n-alkane input in the southern South China Sea. Global Planet. Change 94, 1-12.

Hutchison, C.S., 2005. Geology of NorthWest Borneo: Sarawak, Brunei and Sabah. Elsevier, The Netherlands, 399pp.

Hutchison, C.S., 2010. The North-West Borneo Trough. Mar. Geol. 271, 32-43. https://doi.org/10.1016/j.margeo.2010.01.007.

Jiwarungrueangkul, T., Liu, Z., Stattegger, K., Sang, P. N., 2019. Reconstructing chemical weathering intensity in the Mekong River basin since the Last Glacial Maximum. Paleoceanogr. Paleoclimatol. DOI: 10.1029/2019PA003608.

Kawabe, M., Fujio, S., 2010. Pacific ocean circulation based on observation, J. Oceanogr. 66(3), 389-403.

King, J., Channell, J.E.T., 1991. Sedimentary magnetism, environmental magnetism, and magnetostratigraphy. U.S. National Report to International Union Geodesy and Geophysics. Rev. Geophys. Suppl. 29, pp. 358-370.

King, J.W., Banerjee, S.K., Marvin, J., Özdemir, Ö., 1982. A comparison of different magnetic methods for determining the relative grain size of magnetite in natural materials: some results from lake sediments. Earth Planet. Sci. Lett. 59, 404-419.

Kissel, C., Laj, C., Clemens, S., Solheid, P., 2003. Magnetic Signature of Environmental Changes in the last 1.2 My at ODP Site1146, South China Sea. Mar. Geol. 201, 119132.

Kissel, C., Laj, C., Labeyrie, L., Dokken, T., Voelker, A., Blamart, D., 1999. Rapid climatic variations during marine isotopic stage 3: magnetic analysis of North Atlantic sediments. Earth and Planet. Sci. Lett. 171, 489502.

Kissel C., Laj C., Piotrowski A.M., Goldstein S.L., Hemming S.R., 2008. Millenial scale propagation of Atlantic deep waters to the glacial southern ocean. Paleoceanogr. 23, PA2102, https://doi.org/10.1029/2008PA001624.

Kissel, C., Laj, C., Mulder, T., Wandres, C., Cremer M., 2009. The magnetic fraction: a tracer of deep water circulation in the North Atlantic. Earth and Planet. Sci. Lett., 288 (34), 444-454, https://doi.org/10.1016/j.epsl.2009.10.005.

Kissel, C., Van Toer, A., Laj, C., Cortijo, E., Michel, E., 2013. Variations in the Strength of the North Atlantic Bottom water during Holocene. Earth Planet. Sci. Lett. 369-370, 248-259, http://dx.doi.org/10.1016/j.epsl.2013.03.042.

Kissel, C., Liu, Z., Li, J., Wandres, C., 2016. Magnetic minerals in three Asian rivers draining into the South China Sea: Pearl, Red and Mekong Rivers. Geochem. Geophys. Geosyst. 17, 16781693, https://doi.org/10.1002/2016GC006283.

Kissel, C., Liu, Z., Li, J., Wandres, C., 2017. Magnetic signature of river sediments drained into the southern and eastern part of the South China Sea (Malay Peninsula, Sumatra, Borneo, Luzon and Taiwan). Sediment. Geol. 347, 1020, http://dx.doi.org/10.1016/j.sedgeo.2016.11.007.

Kissel, C., Sarnthein, M., Laj, C., Wang, P.X., Wandres, C., Egli, R., 2018. Magnetic fingerprints of modern sediments in the South China Sea resulting from source to sink processes. Geochem. Geophys. Geosyst. 19, https://doi.org/10.1029/2018GC007571.

Kruiver, P. P., Dekkers, M. J., Heslop, D., 2001. Quantification of magnetic coercivity components by the analysis of acquisition curves of isothermal remanent magnetization, Earth Planet. Sci. Lett., 189, 269–276.

Kuo, N., Zheng, Q., Ho, C. R., 2000. Satellite observation of upwelling along the western coast of the South China Sea. Remote Sens. Environ. 74, 463–470.

Kutzbach, J.E., Liu, X.D., Liu, Z., Chen, G., 2008. Simulation of the evolutionary response of global summer monsoons to orbital forcing over the past 280,000 years. Clim. Dyn. 30, 567–579. http://dx.doi.org/10.1007/s003820070308z.

Laj, C., Wang, PX., Balut, Y., 2005. MD 147/Marco Polo 1 IMAGESXII cruise report. In Les rapports de campagne à la mer, IPEV, ref: OCE/2005/02.

Lan, J., Wang, Y., Cui, F., Zhang, N., 2015. Seasonal variation in the South China Sea deep circulation. J. Geophys. Res. Oceans, 120, 1682–1690, https://doi.org/10.1002/2014JC010413.

Li, L., Wang, H., Li, J., Zhao, M., Wang, P., 2009. Changes in sea surface temperature in western South China Sea over the past 450 ka. Chin. Sci. Bull. 54, 3335-3343.

Li, M., Ouyang, T., Roberts, A. P., Heslop, D., Zhu, Z., Zhao, X., Tian, C., Peng, S., Zhong, H., Peng, X., Qiu, Y., 2018. Influence of sea level change and centennial East Asian monsoon variations on northern South China Sea sediments over the past 36 kyr. Geochem. Geophys. Geosyst. 19, 1674–1689. https://doi.org/10.1029/2017GC007321

Li, N., Yang, X.Q., Peng, J., Zhou, Q., Zhu, Z., 2019. Deepwater bottom current evolution in the northern South China Sea during the last 150 kyr: Evidence from sortable silt grain size and sedimentary magnetic fabric. J. Asian Earth Sci. 171, 78-87. https://doi.org/10.1016/j.jseaes.2017.06.005.

Lisiecki, L., Raymo, M., 2005. A Pliocene-Pleistocene stack of 57 globally distributed benthic $\delta^{18}O$ records. Paleoceanogr. 20, doi:10.1029/2004PA001071.

Liu, J., Chen, Z., Chen, M., Xiang, W. Y., & Tang, X., 2010. Magnetic susceptibility variations and provenance of surface sediments in the South China Sea. Sediment. Geol. 230(12), 77-85. https://doi.org/10.1016/j.sedgeo.2010.07.001

Liu, J., Xiang, R., Chen, Z., Chen, M., Yan, W., Zhang, L., Chen, H., 2013. Sources, transport, and deposition of surface sediments from the South China Sea. Deep-sea Res. I, 71, 92-102. https://doi.org/10.1016/j.dsr.2012.09.006.

Liu, J., Clift, P.D., Yan, W., Chen, Z., Chen, H., Xiang, R., Wang, D., 2014. Modern transport and deposition of settling particles in the northern South China Sea : Sediment trap evidence adjacent to Xisha Trough. Deep-Sea Res. I, 93, 145-155. https://doi.org/10.1016/j.dsr.2014.08.005.

Liu, Q., Kaneko, A. Jilan, S., 2008. Recent Progress in Studies of the South China Sea Circulation. J. Oceanogr., 64, 753762.

Liu, Y., Gao, S., Wang, Y., Yang, Y., Long, J., Zhang, Y., Wu, X., 2014. Distal mud deposits associated with the Pearl River over the northwestern continental shelf of the South China Sea. Mar. Geol. 347, 43–57.

Liu, Z., Colin, C., Trentesaux, A., Blamart, D., Bassinot, F., Siani, G., Sicre, M-A., 2004. Erosional history of the eastern Tibetan Plateau since 190 kyr ago: clay mineralogical and geochemical investigations from the southwestern South China Sea. Mar. Geol., 209, 118, doi:10.1016/j.margeo.2004.06.004

Liu, Z., Stattegger, K., 2014. South China Sea fluvial sediments: An introduction, J. Asian Earth Sci. 79, 507–508.

Liu, Z., Zhao, Y., Colin, C., Stattegger, K., Wiesner, M. G., Huh, C. A., Zhang, Y., Li, X., Sompongchaiyakul, P., You, C.F., Huang, C.Y., Liu, J. T., Sirigan, F. P., Le, K. P., Sathiamurthy, E., Hantoro, W. S., Liu, J., Tuo, S., Zhao, S., Zhou, S., He, Z., Wang, Y., Bunsomboonsakul, S., Li, Y., 2016. Source-to-sink processes of fluvial sediments in the South China Sea. Earth Sci. Rev. 153, 238–273. https://doi.org/10.1016/j.earscirev.2015.08.005

Lowrie, W., 1990. Identification of ferromagnetic minerals in a rock by coercivity and unblocking temperature properties. Geophys. Res. Lett. 17, 159–162.

Mark, D.F., Petraglia, M., Smith, V. C., Morgan, L. E., Barfod, D. N., Ellis, B. S., Pearce, N. J., Pal J.N., Korisettar, R., 2013. A highprecision 40Ar/ 39Ar age for the Young Toba Tuff and dating of ultradistal tephra: Forcing of Quaternary climate and implications for hominin occupation of India. Quat. Geochronol. 21, 90-103, https://doi.org/10.1016/j.quageo.2012.12.004.

Mazaud, A., Sicre, M. A., Ezat, U., Pichon, J.J., Duprat, J., Laj, C., Kissel, C., Beaufort, L., Michel, E., Turon, J.L., 2002. Geomagnetic assisted stratigraphy and SST changes in core MD94103 (southern Indian Ocean): possible implications for NorthSouth climatic relationships around H4. Earth Planet. Sci. Lett, 201, 159-170.

Milliman, J.D., Farnsworth, K.L., Albertin, C.S., 1999. Flux and fate of fluvial sediments leaving large islands in the East Indies. J. Sea Res. 41, 97–107.

Milliman, J.D., Farnsworth, K.L., 2011. River Discharge to the Coastal Ocean: A Global Synthesis. Cambridge University Press, Cambridge (384 pp.).

Nguyen, T.T.H., Zhang, W.G., Li, Z., Li, J., Ge, C., Liu, J.Y., Bai, X.X., Feng, H., Yu, L.Z., 2016. Magnetic properties of sediments of the Red River: effect of sorting on the sourcetosink pathway and its implications for environmental reconstruction. Geochem. Geophys. Geosyst. 17. http://dx.doi.org/10.1002/2015GC006089.

Nguyen, V.L., Ta, T.K.O., Tateishi, M., 2000. Late Holocene depositional environments and coastal evolution of the Mekong River Delta, Southern Vietnam. J. Asian Earth Sci. 18, 427–439.

Ni, Y., Harff, J., Xia, Z., Waniek, J. J., Endler, M., SchulzBull, D. E., 2016. Postglacial mud depocentre in the southern Beibu Gulf: acoustic features and sedimentary environment evolution, in: Clift, P. D., Harff, J., Wu, J., Yan, Q. (Eds) River Dominated Shelf Sediments of East Asian Seas. Geological Society, London, Special Publications, 429, http://doi.org/10.1144/SP429.13

Ninkovich, D., Shackleton, N.J., AbdelMonem, A.A., Obradovich, G., Izett, G., 1978. K–Ar age of the late Pleistocene eruption of Toba, north Sumatra. Nature 276, 574– 577.

Oppo, D., Sun, Y., 2005. Amplitude and timing of seasurface temperature change in the northern South China Sea: Dynamic link to the East Asian monsoon, Geology 33 (10), 785788, https://doi.org/10.1130/G21867.1

Ouyang, T., Appel, E., Jia, G., Huang, N., Zhu, Z., 2013. Magnetic mineralogy and its implication of contemporary coastal sediments from South China. Environ. Earth Sci. 68, 1609–1617. https://doi.org/10.1007/s1266501218541.

Ouyang, T., Tian C., Zhu, Z., Qiu, Y., Appel, E., Fu, S., 2014a. Magnetic characteristics and its environmental implications of core YSJD86GC sediments from the southern South China Sea, Chin. Sci. Bull. 59(25), 31763187. https://doi.org/10.1007/s1143401404388.

Ouyang, T., Heslop, D., Roberts, A. P., Tian, C., Zhu, Z., Qiu, Y., Peng, X., 2014b. Variable remanence acquisition efficiency in sediments containing biogenic and detrital magnetites: Implications for relative paleointensity signal recording, Geochem. Geophys. Geosyst., 15, 2780–2796, doi:10.1002/2014GC005301.

Ouyang, T., Li, M., Zhao, X., Zhu, Z., Tian, C., Qiu, Y., Peng, X., Hu Q., 2016. Sensitivity of Sediment Magnetic Records to Climate Change during Holocene for the Northern South China Sea. Front. Earth Sci. 4:54. https://doi.org/10.3389/feart.2016.00054.

Ouyang, T., Li, M., Appel, E., Fu, S., Jia, G., Li, W., Zhu, Z., 2017. Magnetic properties of surface sediments from the Pearl River Estuary and its adjacent waters: Implication for provenance. Marine Geol. 390, 80–88. https://doi.org/10.1016/j.margeo.2017.06.002.

Özdemir, Ö., Dunlop, D. J., 1996. Thermoremanence and Néel temperature of goethite. Geophys. Res. Lett., 23(9), 921-924. https://doi.org/10.1029/96GL00904.

Panagos P., Jones A., Bosco C., Senthil Kumar P.S., 2011. European digital archive on soil maps (EuDASM): Preserving important soil data for public free access, Int. J. Digital Earth, 4 (5), 434-443.

Peters, C., and Dekkers, M.J., 2003. Selected room temperature magnetic parameters as a function of mineralogy, concentration and grain size. Phys. Chem. Earth 28, 659–667.

Qu, T., H. Mitsudera T. Yamagata, 2000. Intrusion of the North Pacific waters into the South China Sea. J. Geophys. Res., 105(C3), 6415–6424.

Qu, T., J. B. Girton, J. A. Whitehead, 2006. Deepwater overflow through Luzon Strait, J. Geophys. Res., 111, C01002, https://doi.org/10.1029/2005JC003139.

Ridd, M. F., Barber, A. J., Crow, M. J., 2011. The Geology of Thailand. The Geological Society, London, pp 626.

Snowball, I., Thompson, R., 1990. A mineral magnetic study of Holocene sedimentation in Lough Catherine, Northern Ireland. Boreas, 19, 127-146.

Staub, J.R., Among, H.L., Gastaldo, R.A., 2000. Seasonal sediment transport and deposition in the Rajang River delta, Sarawak, East Malaysia. Sediment. Geol. 133, 149–264.

Staub, J.R., Esterle, J.S., 1992. Provenance and sediment dispersal in the Rajang River delta/coastal plain system, Sarawak, East Malaysia. Sediment. Geol. 85, 191201.

Steinke, S., Chiu, H.Y., Yu, P.S., Shen, C. C., Erlenkeuser, H., Löwemark, L., Chen, M.T., 2006. On the influence of sea level and monsoon climate on the southern South China Sea freshwater budget over the last 22,000 years. Quat. Sci. Rev., 25(1314), 1475-1488.

Steinke, S., Hanebuth, T. J.,Vogt, C., Stattegger,K., 2008. Sea level induced variations in clay mineral composition in the southwestern South China Sea over the past 17000 years. Mar. Geol., 250, 199-210.

Sun, X., Li, X., Beug, H.J., 1999. Pollen distribution in hemipelagic surface sediments of the South China Sea and its relation to modern vegetation distribution, Mar. Geol., 156 (14). https://doi.org/10.1016/S00253227(98)001807

Sun, X., Luo, Y., Huang, F., Tian, J., Wang, P.X., 2003. Deep sea pollen from the South China Sea: Pleistocene indicators of East Asian monsoon. Mar. Geol., 201(13), 97118.

Szczuciński, W., Stattegger, K., Scholten, J., 2009. Modern sediments and sediment accumulation rates on the narrow shelf off central Vietnam, South China Sea. GeoMar. Lett., 29, 47–59.

Szczuciński, W., Jagodziński, R., Hanebut, T.J.J, Stattegger, K., Wetzel A., Mitręga, M., Unverrich, D., Van Phach, P., 2013. Modern sedimentation and sediment dispersal pattern on the continental shelf off the Mekong River delta, South China Sea. Global Planet. Change, 110, 195–213. https://doi.org/10.1016/j.gloplacha.2013.08.019

Ta, T.K.O., Nguyen, V.L., Tateishi, M., Kobayashi, I., Tanabe, S., Saito, Y., 2002. Holocene delta evolution and sediment discharge of the Mekong River, southern Vietnam. Quat. Sci. Rev. 21 (16–17), 1807–1819.

Tarling, D.H., Hrouda, F., 1993. The Magnetic Anisotropy of Rocks. Chapman and Hall, London. 2177pp.

Thanh T.V., Hieu, P.T., Minh, P., Nhuan, D.V., Thuy N.T.B., 2019. Late Permian-Triassic granitic rocks of Vietnam: the Muong Lat example. Int. Geol. Rev., https://doi.org/10.1080/00206814.2018.1561335.

Tian, J., Wang P.X., Cheng, X., Li, Q., 2002. Astronomically tuned Plio-Pleistocene benthic $\delta^{18}O$ record from South China Sea and Atlantic Pacific comparison. Earth Planet. Sci. Lett., 203(34), 10151029, https://doi.org/10.1016/S0012821X(02)009238.

Tian, J Zhao, Q., Wang, P.X., Li, Q., Cheng, X., 2008. Astronomically modulated Neogene sediment records from the South China Sea. Paleoceanogr., 23, PA3210, https://doi.org/10.1029/2007PA001552.

Tian, J., Huang, E., Pak, D.K., 2010. East Asian winter monsoon variability over the last glacial cycle: insights from a latitudinal seasurface temperature gradient across the South China Sea. Palaeogeogr., Palaeoclimatol., Palaeoecol. 292, 319-324.

Tian, J.W., Yang, Q., Liang, X., Xie, L., Hu, D., Wang, F., Qu T.D., 2006. Observation of Luzon Strait transport. Geophys. Res. Lett. 33, 19607, doi: 10.1029/2006GL026272.

Tian, J.W., Qu, T.D., 2012. Advances in research on the deep South China Sea circulation. Chinese Sci. Bull. 57 (24), 3115-3120. https://doi.org/10.1007/s114340125269x.

Voris, H.K., 2000. Maps of Pleistocene sea levels in Southeast Asia: shorelines, river systems and time durations, J. Biogeogr., 27, 1153-1167. https://doi.org/10.1046/j.1365-2699.2000.00489.x.

Wan, S., Jian, Z., 2014. Deep water exchanges between the South China Sea and the Pacific since the last glacial period, Paleoceanogr., 29, 1162-1178, https://doi.org/10.1002/2013PA002578.

Wan, S., Toucanne, S., Clift, P. D., Zhao, D., Bayon, G., Yu, Z., Cai, G., Yin, X., Révillon, S., Wang, D., Li, A., Li, T., 2015. Human impact overwhelms long-term climate control of weathering and erosion in southwest China. Geology. https://doi.org/10.1130/G36570.1.

Wan, S., Jian, Z., Dang, H., 2018. Deep hydrography of the South China Sea and deep water circulation in the Pacific since the Last Glacial Maximum. Geochem., Geophys., Geosyst., 19, 1447–1463. https://doi.org/10. 1029/2017GC007377.

Wang, C., Liang, X., Foster, D. A., Liang, X., Zhang, L., Su, M., 2019. Provenance and drainage evolution of the Red River revealed by Pb isotopic analysis of detrital K-feldspar. Geophys. Res. Lett., 46, 6415-6424. https://doi.org/10.1029/2019GL083000.

Wang, G., Xie, S.P., Qu, T., Huang, R.X., 2011. Deep South China Sea circulation. Geophys. Res. Lett., 38, L05601, https://doi.org/10.1029/2010GL046626.

Wang, L., Sarnthein, M., Erlenkeuser, H., Grimalt, J., Grootes, P., Heilig, S., Ivanova, E., Kienast, M., Pelejero, C., Pflaumann, U., 1999. East Asian monsoon climate during the Late Pleistocene: high-resolution sediment records from the South China Sea. Mar. Geol., 156, 245-284.

Wang, P. X., Prell, W. L., Blum, P., 2000. Proc. ODP, initial reports, 184, College Station, TX (Ocean Drilling Program). https://doi.org/10.2973/odp.proc.ir.184.2000.

Wang, P.X., Li, Q., 2009. The South China Sea, Paleoceanogr. and Sedimentol. Springer, Netherlands, Dordrecht (506 pp.).

Wang, P.X., Li, Q., Tian, J., Jian, Z., Liu, C., Li, L., Ma, W., 2014. Long-term cycles in the carbon reservoir of the Quaternary ocean: a perspective from the South China Sea. Nat. Sci. Rev. 1, 119-143. doi: 10.1093/nsr/nwt028.

Wang P.X., Li, Q., Tian, J., He, J., Jian, Z., Ma, W., Dang H., 2016. Monsoon influence on planktic $\delta^{18}O$ records from the South China Sea. Quat. Sci. Rev. 142, 2639. https://doi.org/10.1016/j.quascirev.2016.04.009.

Wang, P. X., Wang, B., Cheng, H., Fasullo, J., Guo, Z. T., Kiefer, T., Liu, Z. Y., 2017. The global monsoon across time scales: Mechanisms and outstanding issues. Earth Sci. Rev. 174, 84121.

Wang, X.M., Sun, X.J., Wang, P.X., Stattegger, K., 2009. Vegetation on the Sunda Shelf, South China Sea, during the Last Glacial Maximum, Palaeogeogr., Palaeoclimatol., Palaeoecol., 278, (1–4), 88-97. https://doi.org/10.1016/j.palaeo.2009.04.008

Weeks, R., Laj, C., Endignoux, L., Fuller, M., Roberts, A., Manganne, R., Blanchard, E., Goree, W., 1993. Improvements in long-core measurements techniques: applications in palaeomagnetism and palaeoceanography, Geophys. J. Int., 114, 651662.

Williams, P.R., Johnston C.R., Almond, R.A., Simamora, W.H., 1988. Late Cretaceous to Early Tertiary Structural elements of West Kalimantan. Tectonophys. 148, 279297.

Wyrtki, K., 1961. Physical oceanography of the Southeast Asian waters, Scientific results of marine investigations of the South China Sea and the Gulf of Thailand, NAGA Report 2, Scripps Institution of Oceanography, La Jolla, CA, pp. 1–195.

Xie, S.P., Q. Xie, D. Wang, W. T. Liu, 2003. Summer upwelling in the South China Sea and its role in regional climate variations, J. Geophys. Res., 108(C8), 3261, https://doi.org/10.1029/2003JC001867.

Yamazaki, T., M. Ikehara, 2012. Origin of magnetic mineral concentration variation in the Southern Ocean, Paleoceanogr., 27, PA2206, https://doi.org/10.1029/2011PA002271.

Yang, Q., Tian, J., Zhao, W., 2010. Observation of Luzon Strait transport in summer 2007, Deep-Sea Res. I, 57, 670676.

Yang, X.Q., Rodney, G., Zhou, H.Y., Yang, J., 2008. Magnetic properties of sediments from the Pearl River Delta, South China: paleoenvironmental implications. Sci. China Earth Sci. 51, 5566. https://doi.org/CNKI:SUN:JDXG.0.200801007.

Yang X.Q., Heller, F., Wu, N., Yang, J., Su Z.H., 2009. Geomagnetic paleointensity dating of South China Sea sediments for the last 130 kyr, Earth Planet. Sci. Lett., 284, 258266. https://doi.org/ 10.1016/j.epsl.2009.04.035.

Yang, X.Q., Peng, X., Qiang, X., Li, N. Zhou, Q., Wang, Y., 2016. Chemical Weathering Intensity and Terrigenous Flux in South China during the Last 90,000 Years—Evidence from Magnetic Signals in Marine Sediments. Front. Earth Sci. 4(47). https://doi.org/10.3389/feart.2016.00047.

Yao, Y.T., Harff J., Meyer, M., Zhan, W.H., 2009. Reconstruction of paleocoastlines for the northwestern South China Sea since the Last Glacial Maximum. Sci. China Ser. D Earth Sci., 52, 11271136, https://doi.org/10.1007/s1143000900988

Yim, W.W.S., Huang, G., Chana, L.S., 2004. Magnetic susceptibility study of Late Quaternary inner continental shelf sediments in the Hong Kong SAR, China. Quat. Int. 117, 41–54. https://doi.org/10.1016/S10406182(03)001150.

Zhang N, Lan J, Cui F., 2014. The shallow meridional overturning circulation of the South China Sea. Ocean Sci. Discussions 11, 1191-1212. doi:10.5194/osd-11-1191-2014.

Zhang, Y.G., Ji, J., Balsam, W. L., Liu, L., Chen, J., 2007. High resolution hematite and goethite records from ODP 1143, South China Sea: Coevolution of monsoonal precipitation and El Niño over the past 600,000 years. Earth Planet. Sci. Lett. 264, 136-150. https://doi.org/10.1016/j.epsl.2007.09.022.

Zhao, M., Huang, C.Y., Wang, C.C., Wei, G., 2006. A millennial scale U37K' sea surface temperature record from the South China Sea (8°N) over the last 150 kyr: Monsoon and sea level influence. Palaeogeogr. Palaeoclimatol. Palaeoecol. 236(1), 3955. https://doi.org/: 10.1016/j.palaeo.2005.11.033

Zhao M., Shao, L., Liang, J., Li, Q., 2015. No Red River capture since the late Oligocene: Geochemical evidence from the Northwestern South China Sea. Deep Sea Research Part II: topical studies in oceanography, 122, 185-194, https://doi.org/10.1016/j.dsr2.2015.02.029.

Zhao S.H., Liu Z.F., Chen Q., Wang X.X., Shi J.N., Jin H.Y., Liu J.J., Jian Z.M., 2017. Spatio temporal variations of deep sea sediment components and their fluxes since the last glaciation in the northern South China Sea. Sci. China Earth Sci., 60: 1368–1381. https://doi.org/10.1007/s1143001690586.

Zhao, Y., Liu, Z., Zhang, Y., Li, J., Wang, M, Wang W., Xu, J., 2015. *In situ* observation of contour currents in the northern South China Sea: Applications for deep water sediment transport. Earth Planet. Sci. Lett., 430, 477–485. https://doi.org/10.1016/j.epsl.2015.09.008

Zheng, X.F., Kao, S.J., Chen, Z., Menviel, L., Chen, H., Du, Y., Wan, S.M., Yan, H., Liu, Z.H., Zheng, L.W., Wang, S.H., Li, D.W., Zhang, X., 2016. Deepwater circulation variation in the South China Sea since the last glacial. Geophys. Res. Lett. 43. https://doi.org/ 10.1002/2016GL07034.

Zhong Y., Chen, Z., Li, L., Liu, J., Li, G., Zheng, X., Wang, S., Mo, A., 2017. Bottom water hydrodynamic provinces and transport patterns of the northern South China Sea: Evidence from grain size of the terrigenous sediments. Cont. Shelf Res., 140, 11–26.

Zhu, Y. Fang, G., Wei, Z., Wang, Y., Teng, F., Qu, T., 2016. Seasonal variability of the meridional overturning circulation in the South China Sea and its connection with interocean transport based on SODA2.2.4. J. Geophys. Res. Oceans, 121, 3090–3105. https://doi.org/10.1002/2015JC011443.

Figure captions

Fig. 1. Geological and oceanic context of the South China Sea. All the back ground maps are from GeoMapApp. a) Geological map of Southeast Asia surrounding the SCS, modified after Liu et al. (2016). 1, 2, 3, 4 are for Quaternary, Cenozoic, Mesozoic and Paleozoic sedimentary rocks, respectively. 4 and 5 are for extrusive and intrusive igneous rocks, respectively. The light orange arrows with numbers indicate the pre-dam fluvial sediment discharge (in 10^6 t/yr) (Milliman and Farnsworth, 2011 ; Liu et al., 2016). The numbers have been modified for Sumatra and Borneo with respect to Liu et al. (2016) to be consistent with the direct observations from rivers (Cecil et al., 2003; Staub et al., 2000; Hiscott, 2001). The limits of the catchment basin of the Pearl, Red and Mekong rivers are highlighted by black lines. b : location of the studied and discussed sites. Grey dots are for river samples (Kissel et al., 2016 ; 2017), white dots for core-top samples (Kissel et al., 2018), blue and red dots indicate the cores we use in this study, the blue dots are for the cores we quote from published articles, red dots are for the cores, the results of which are reported here for the first time. The dots with thick lines are for cores exceeding 130 ka in age. c) and d) Schematic distribution of the surface currents during boreal winter in c) (dark continuous lines), boreal summer in d) (dashed lines) and of deep currents (thick blue line)(after Hu et al., 2000; Qu et al., 2006; G. Wang et al., 2011). On both maps, the limits of the catchment basin of the Pearl, Red and Mekong rivers are highlighted by yellow lines.

Fig. 2. Synthetic scheme of the main magnetic properties reported in the articles published so far and obtained from sedimentary cores collected in the SCS together with the interpretation drawn by the authors. The location of the cores can be found in Fig. 1 and in Table 1 together with the reference of the corresponding articles. Below the core labels the magnetic proxies

reported in these articles are mentioned with a color code (MM in light orange: Magnetic mineralogy; MC in dark orange: Magnetic concentration; MG in dark pink: magnetic grain size; MA in brown: magnetic anisotropy). The non-magnetic proxies mentioned in these articles are reported with another color code (SG in light green: sedimentary grain size (often sortable silt); ME in green: major elements; Cl in dark green: clay composition). The interpretation given by the authors are reported for each core versus time with another color code: EASM (EAWM) for East Asian Summer (Winter) Monsoon; BC for bottom current. The time periods are: MPT: Mid-Pleistocene transition; G/IG: alternations glacial/interglacial; LGM: Last Glacial Maximum; H1: Heinrich event 1; B/A: Bolling/Alerod; YD: younger Dryas; EH: early Holocene.

Fig. 3. Distribution of the S-ratio illustrated with a color code both in river sediments (large dots; Kissel et al., 2016; 2017) and in core-tops (small dots, Kissel et al., 2018). The map was obtained using GeoMapApp.

Fig. 4. Bulk magnetic parameters reported versus time for all the studied cores. IRM and ARM were normalized around the same mean value as the low field susceptibility (for true values, see Table 3).

Fig. 5. S-ratio versus age for each core (in blue with respect to the vertical blue scale). The black dots (vertical black scales) are for the percentage of magnetization remaining after heating at 600°C along the axis magnetized at 1T with respect to the IRM at room temperature (IRM$_{1T@600°C}$/total IRM$_{@20°C}$ (%))(see Table 2 and text).

Fig. 6. Results of the thermal demagnetization of the 3-axes IRM. a to c) Examples of thermal demagnetization of three axes-IRM in three cores illustrating the southern group (a), the central group (b) and the northern group (c). In each case, the insert is a zoom on the last part of the demagnetization (between 500 and 700°C). The vertical scales are the percentages of magnetization along each axis divided by the total IRM, the horizontal axis is the temperature (°C). d) contribution in percentage of magnetization remaining along each axis (see symbols) after thermal demagnetization at 600°C with respect to the total IRM at room temperature ($IRM_{xT@600°C}$/total $IRM_{@20°C}$) reported versus the contribution (in %) of the magnetization along each axis to the total IRM at room temperature ($IRM_{xT@20°C}$/total $IRM_{@20°C}$).

Fig. 7. Magnetic grain size illustrated by the two ratios ARM/κ (brown curves) and ARM/IRM (green curves), each on their own vertical scale (ARM/IRM ratio have been multiplied by 100). The cores from the south are presented on the left column, the one from the central group in the center and the ones form the northern group, on the right hand side.

Fig. 8. Hysteresis parameters reported as Mrs/Ms versus Bcr/Bc on a Day diagram (Day et al., 1977) revised by Dunlop (2002). SP, SD, PSD and MD are for superparamagnetic, single domains, pseudo-single domains and multi-domains, respectively. The percentages reported on each mixing curve are from Dunlop (2002). Left hand side: core samples, right hand side: river samples

Fig. 9. Examples of decomposition of the IRM acquisition curves into cumulative Log-Gaussian (CLG) components (using the software proposed by Kruiver et al., 2001). a and f: gradient acquisition curves obtained for a sample (left) from the north and a sample (right) from the south, both at around 125 kyr. The pink, green, turquoise and red curves correspond

to CLG1, CLG2, CLG3 and CLG4, respectively. The small blue squares are for the data and the thick red line is the sum of the components. b to j: different parameters reported versus age for both cores (ODP site 1145 from the north on the left and MD01-2393 from the south on the right). These different parameters are the magnetic grain size illustrated by ARM/IRM ratio (b and g); the contribution (in %) of the different CLG components to the IRM (c and h), the dispersion parameter of the different CLG components (d and i) and the median acquisition fields B1/2 (e and j). In all these diagrams the pink curves with diamonds are for CLG1, the green curves with squares are for CLG2; the turquoise curves with triangles are for CLG3 and the orange curve with crosses are for CLG4. The light blue vertical rectangles are for full glacial stages.

Fig. 10. Magnetite grain size fluctuations (ARM/IRM) reported on the same scale for all cores versus age. The oxygen isotopic stack LR04 from benthic foraminifera (Lisiecki and Raymo, 2005) is also reported as a guide for climatic stages. The light blue vertical rectangles are for full glacial stages.

Fig. 11. S-ratio all reported on the same scale versus time. For comparison, the average S-ratio obtained from river samples (Kissel et al., 2016; 2017) are reported on the left hand side (LZ: Luzon; TW: Taiwan; PR: Pearl River; RR: Red River; MR: Mekong River, NW B: NW Borneo; Ma: Malaysia Peninsula) with their 1σ dispersion. The oxygen isotopic stack LR04 from benthic foraminifera (Lisiecki and Raymo, 2005) is also reported as a guide for climatic stages. The light blue vertical rectangles are for full glacial stages.

Fig. 12. Variations of the S-ratio in the southern and northern basins as measured in the longest cores (ODP 1143 and 1145, respectively) covering the last 900 ka. The LR04 stack

(Lisiecki and Raymo, 2005) is given as a guide for the climatic stages in (a). The two S-ratio records from southern ODP site 1143 (b) and northern ODP site 1145 (c) were used to calculate the ΔS-ratio between the north and the south (d). In (d), the 100 kyr and long-term polynomial filtering are also reported as grey and black curves. The ΔS-ratio is compared in (e) to the benthic $\delta^{13}C$ record from the western equatorial Pacific (Dang et al., in press) and in (f) to the coarse fraction index produced by Bassinot et al. (1994). The light yellow vertical rectangles are for interglacial stages and the green one is for the $\delta^{13}C$ max II coinciding with the lowest carbonate dissolution and lowest ΔS-ratio, all illustrating enhanced deep-sea circulation.

Table captions:

Table 1. Geographic coordinates of the cores mentioned in this article. Top part : new cores investigated here organized from north to south, bottom part : cores on which published magnetic data have been obtained and which are mentioned in the text (see Figure 1b for the map).

Table 2. Main magnetic parameters mentioned in this article and their respective meaning.

Table 3. Range of variations of various magnetic parameters in the new cores investigated in this paper. For each parameter and each core, the maximum and minimum values are given together with the mean value all over the last climatic cycle (and the 1σ deviation)

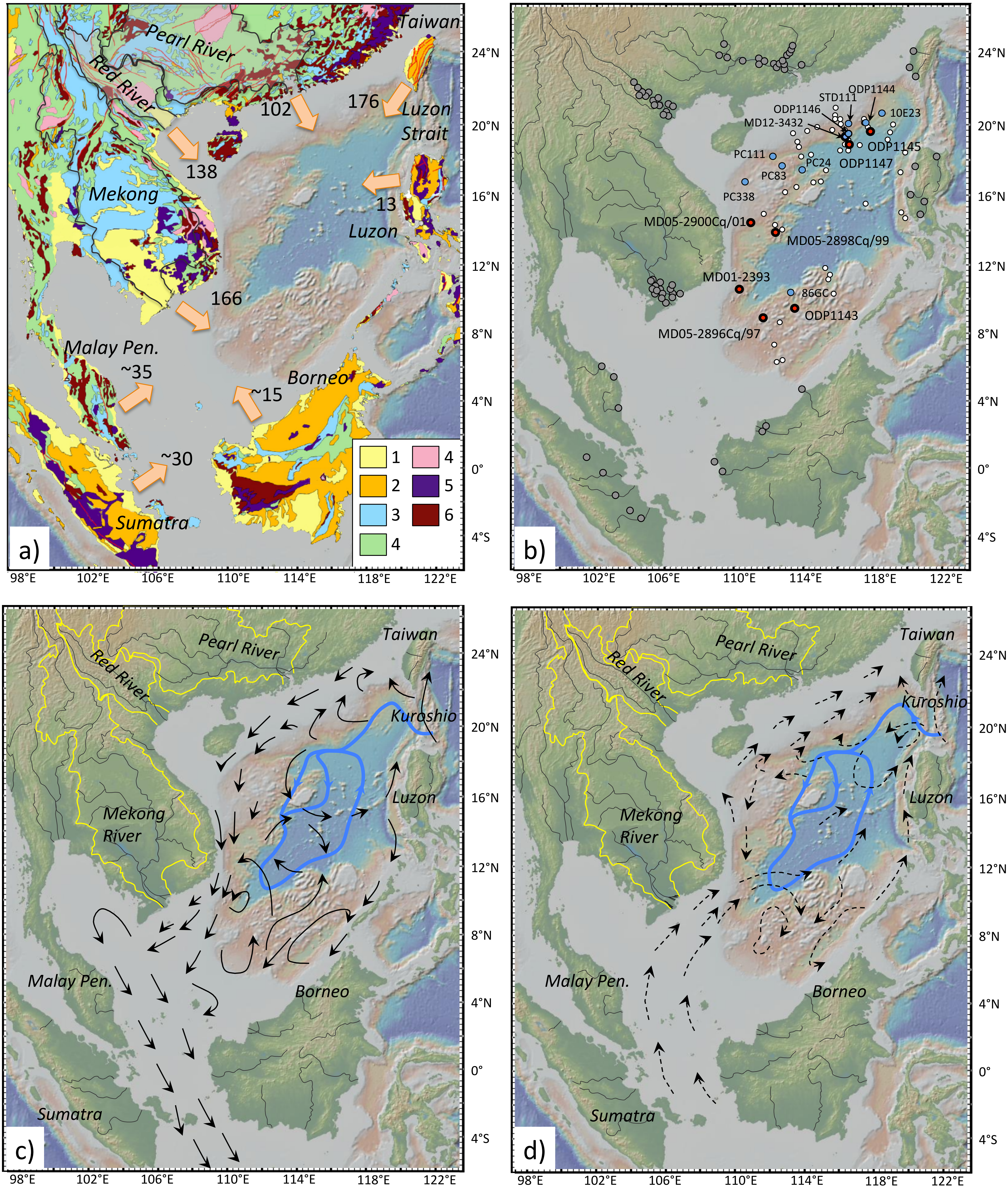

a)
Taiwan
Pearl River
Red River
102
176
Luzon Strait
138
Mekong
13
Luzon
166
Malay Pen.
~35
~15
Borneo
~30
Sumatra
1
2
3
4
4
5
6
b)
ODP1144
STD111
10E23
ODP1146
MD12-3432
ODP1145
PC111
PC24
ODP1147
PC83
PC338
MD05-2900Cq/01
MD05-2898Cq/99
MD01-2393
86GC
ODP1143
MD05-2896Cq/97
c)
Kuroshio
Mekong River
d)
24°N
20°N
16°N
12°N
8°N
4°N
0°
4°S
98°E
102°E
106°E
110°E
114°E
118°E
122°E

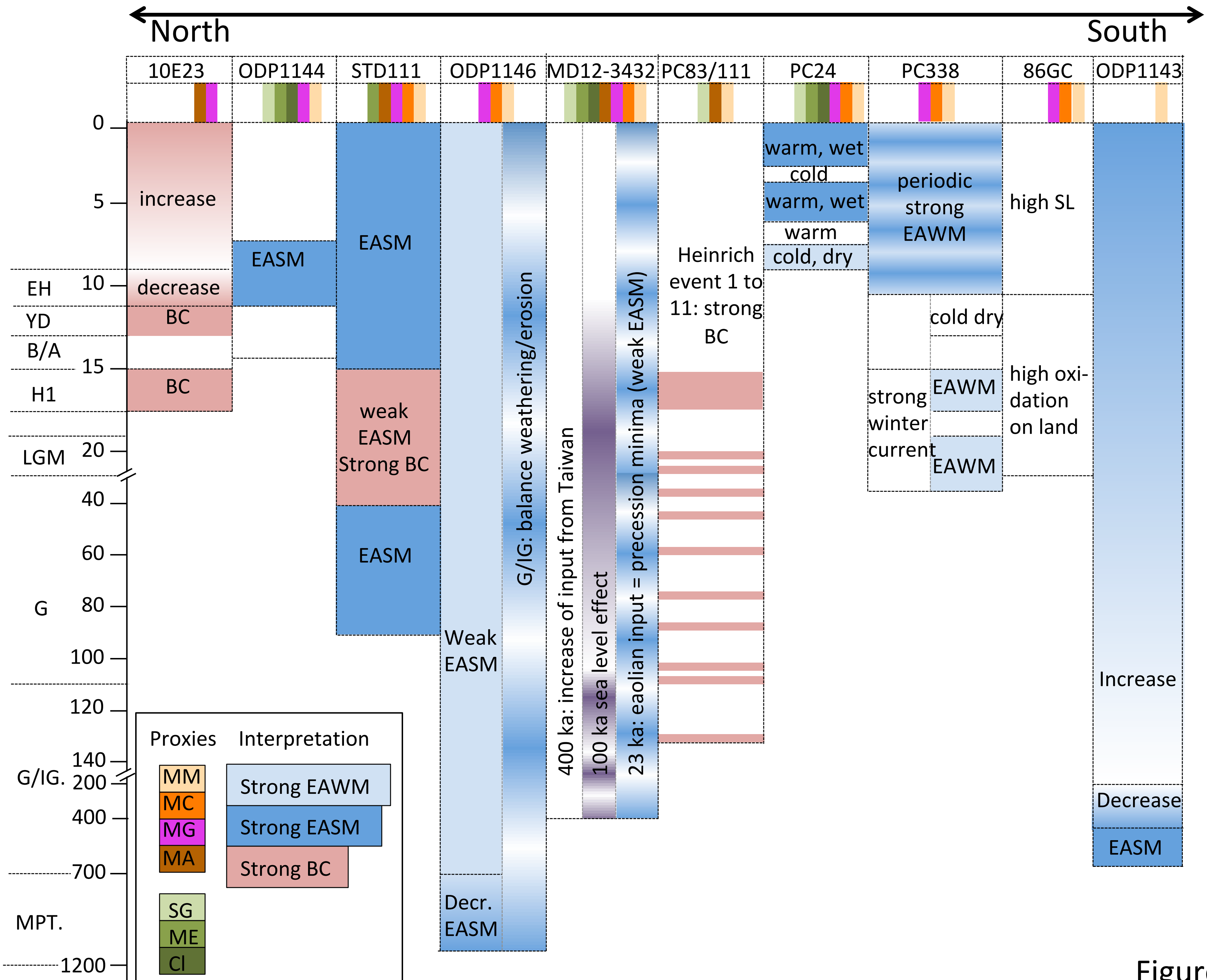
North
South
10E23
ODP1144
STD111
ODP1146
MD12-3432
PC83/111
PC24
PC338
86GC
ODP1143
0
5
10
15
20
40
60
80
100
120
140
200
400
700
1200
EH
YD
B/A
H1
LGM
G
G/IG.
MPT.
increase
decrease
BC
BC
EASM
EASM
weak EASM Strong BC
EASM
Weak EASM
Decr. EASM
G/IG: balance weathering/erosion
400 ka: increase of input from Taiwan
100 ka sea level effect
23 ka: eaolian input = precession minima (weak EASM)
Heinrich event 1 to 11: strong BC
warm, wet
cold
warm, wet
warm
cold, dry
periodic strong EAWM
cold dry
strong winter current
EAWM
EAWM
high SL
high oxi-dation on land
Increase
Decrease
EASM
Proxies
Interpretation
MM
MC
MG
MA
SG
ME
Cl
Strong EAWM
Strong EASM
Strong BC

Figure 2

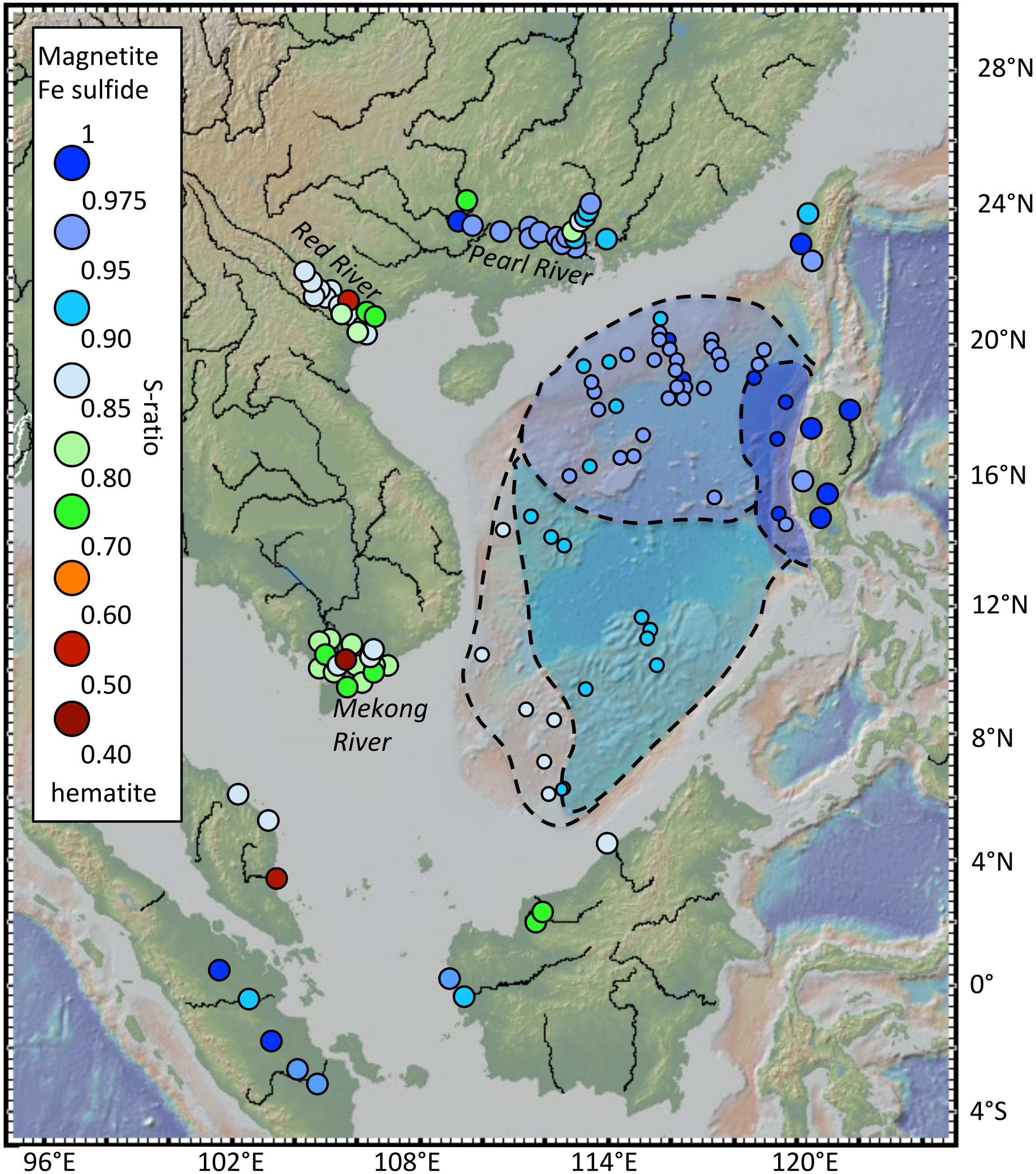

Magnetite
Fe sulfide
1
0.975
0.95
0.90
0.85
0.80
0.70
0.60
0.50
0.40
hematite
S-ratio
Red River
Pearl River
Mekong
River
28°N
24°N
20°N
16°N
12°N
8°N
4°N
0°
4°S
96°E
102°E
108°E
114°E
120°E

Figure 3

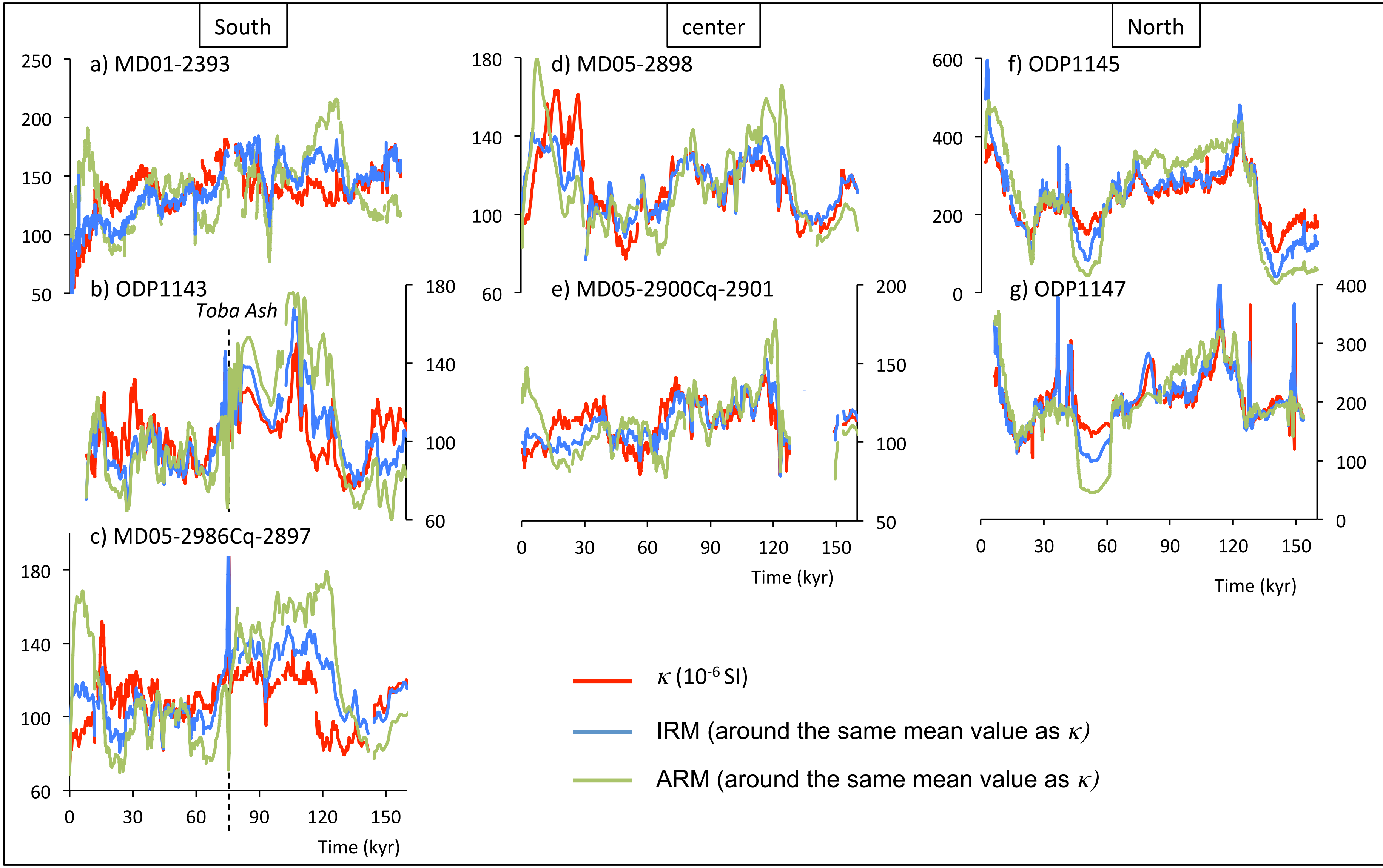
South
center
North
a) MD01-2393
b) ODP1143
c) MD05-2986Cq-2897
d) MD05-2898
e) MD05-2900Cq-2901
f) ODP1145
g) ODP1147
Toba Ash
250
200
150
100
50
180
140
100
60
180
140
100
60
180
140
100
60
200
150
100
50
600
400
200
0
400
300
200
100
0
0
30
60
90
120
150
Time (kyr)
κ (10-6 SI)
IRM (around the same mean value as κ)
ARM (around the same mean value as κ)

Figure 4

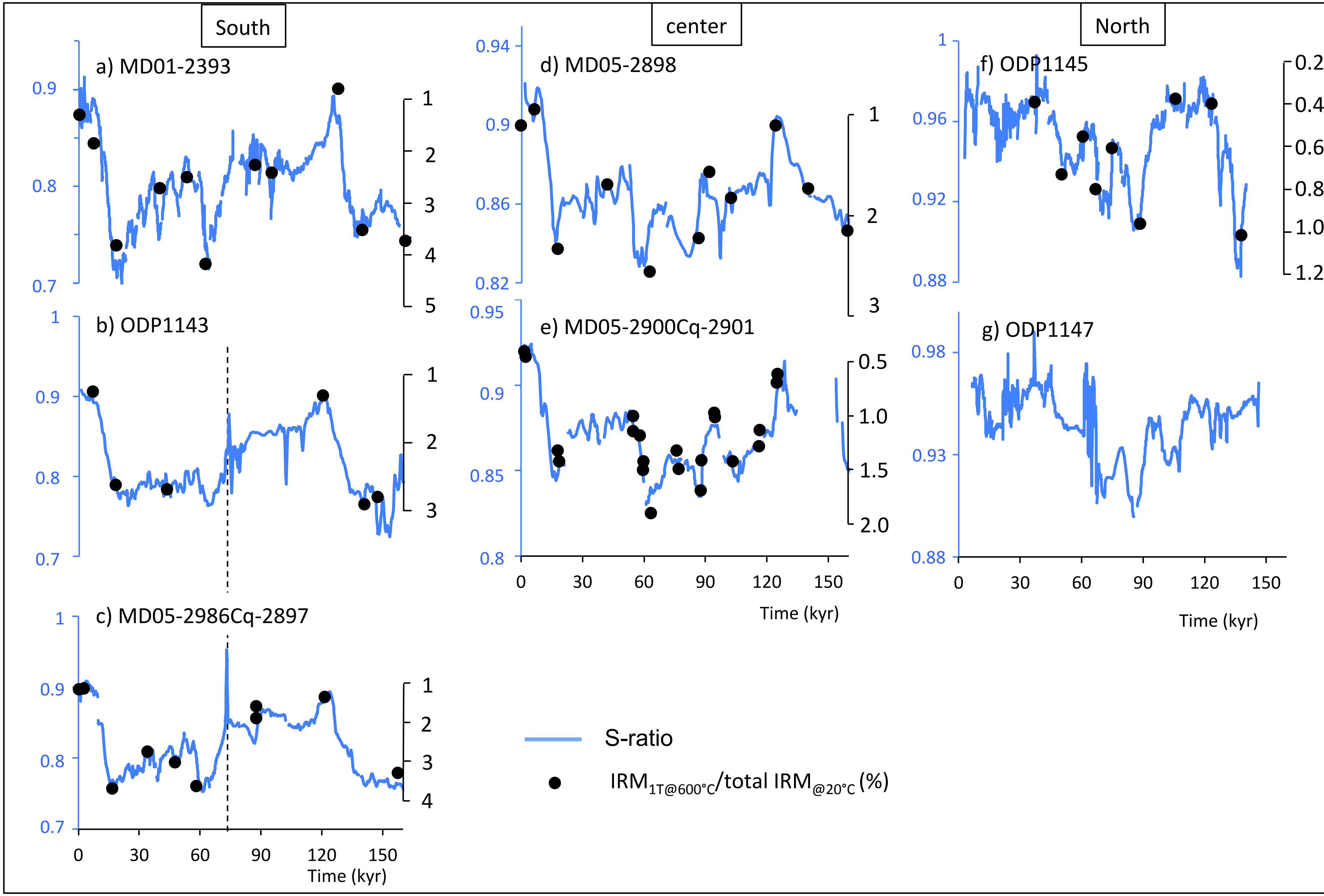

South
center
North
a) MD01-2393
b) ODP1143
c) MD05-2986Cq-2897
d) MD05-2898
e) MD05-2900Cq-2901
f) ODP1145
g) ODP1147
Time (kyr)
Time (kyr)
Time (kyr)
S-ratio
IRM$_{1T@600°C}$/total IRM$_{@20°C}$ (%)

Figure 5

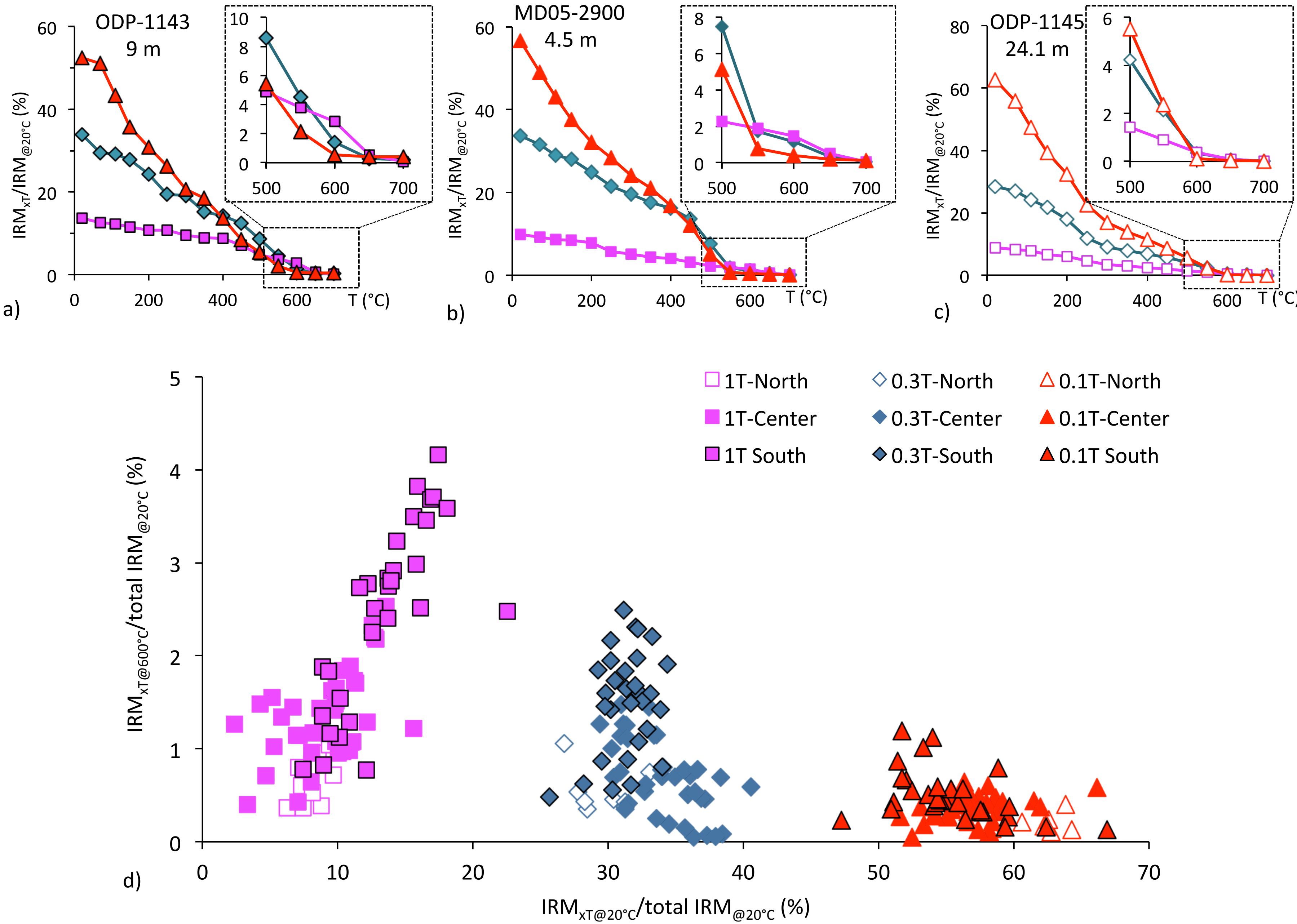

ODP-1143
9 m
MD05-2900
4.5 m
ODP-1145
24.1 m
a)
b)
c)
d)
T (°C)
IRM$_{xT}$/IRM$_{@20°C}$ (%)
1T-North
1T-Center
1T South
0.3T-North
0.3T-Center
0.3T-South
0.1T-North
0.1T-Center
0.1T South
IRM$_{xT@600°C}$/total IRM$_{@20°C}$ (%)
IRM$_{xT@20°C}$/total IRM$_{@20°C}$ (%)

Figure 6

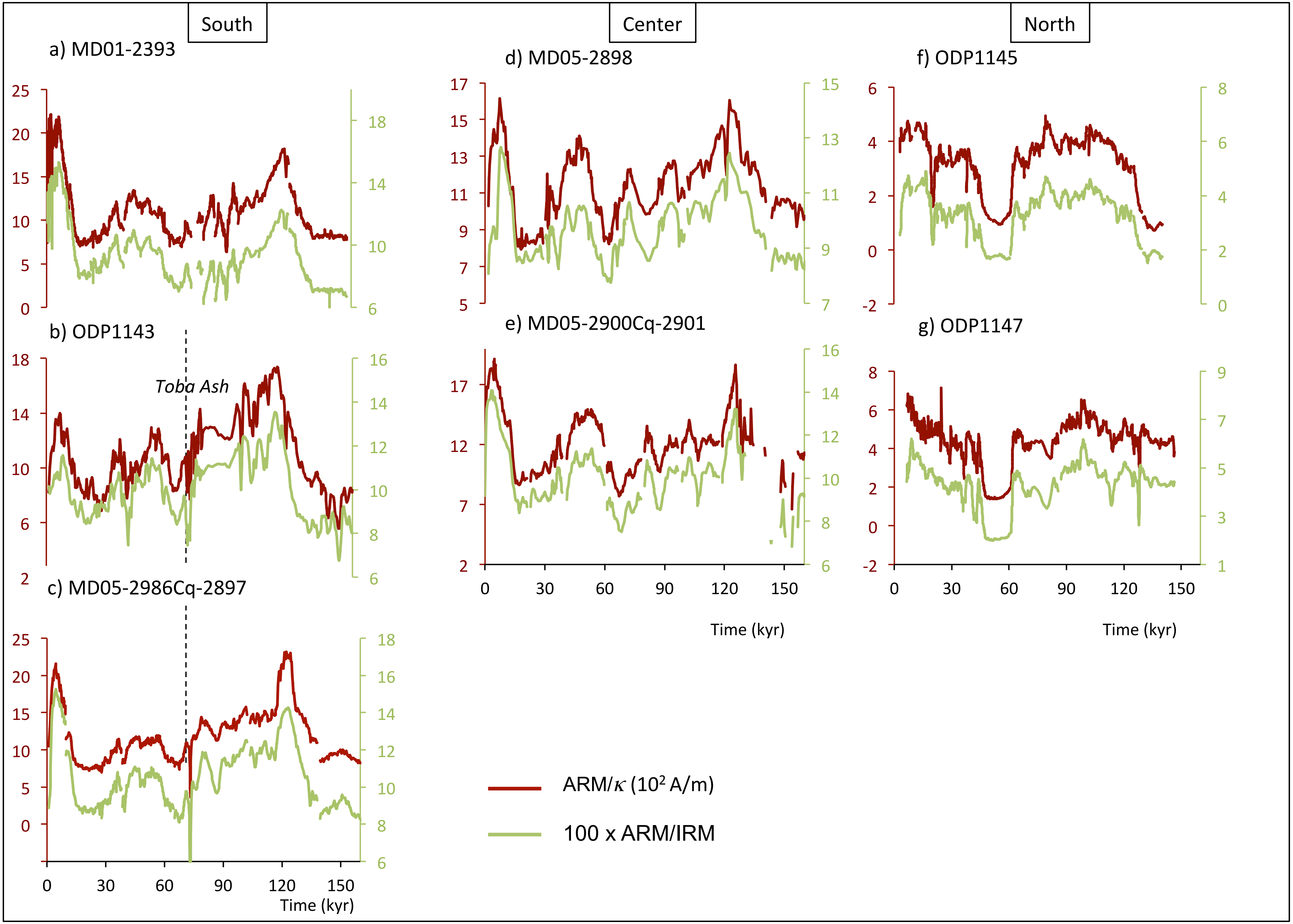

South
Center
North
a) MD01-2393
b) ODP1143
c) MD05-2986Cq-2897
d) MD05-2898
e) MD05-2900Cq-2901
f) ODP1145
g) ODP1147
Toba Ash
Time (kyr)
ARM/κ (10² A/m)
100 x ARM/IRM

Figure 7

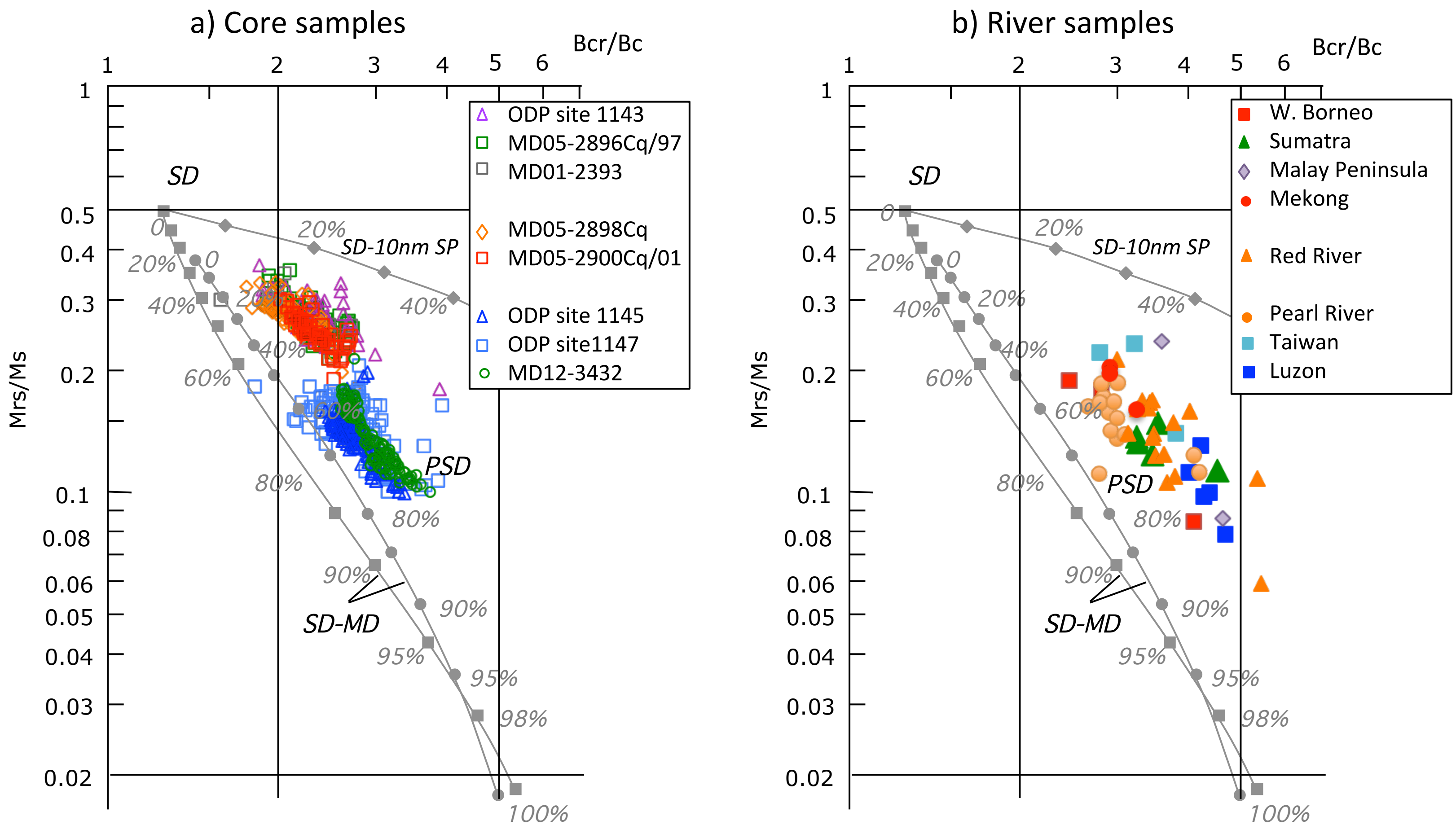

a) Core samples
b) River samples
Bcr/Bc
Mrs/Ms
SD
PSD
SD-MD
SD-10nm SP
ODP site 1143
MD05-2896Cq/97
MD01-2393
MD05-2898Cq
MD05-2900Cq/01
ODP site 1145
ODP site1147
MD12-3432
W. Borneo
Sumatra
Malay Peninsula
Mekong
Red River
Pearl River
Taiwan
Luzon

Figure 8

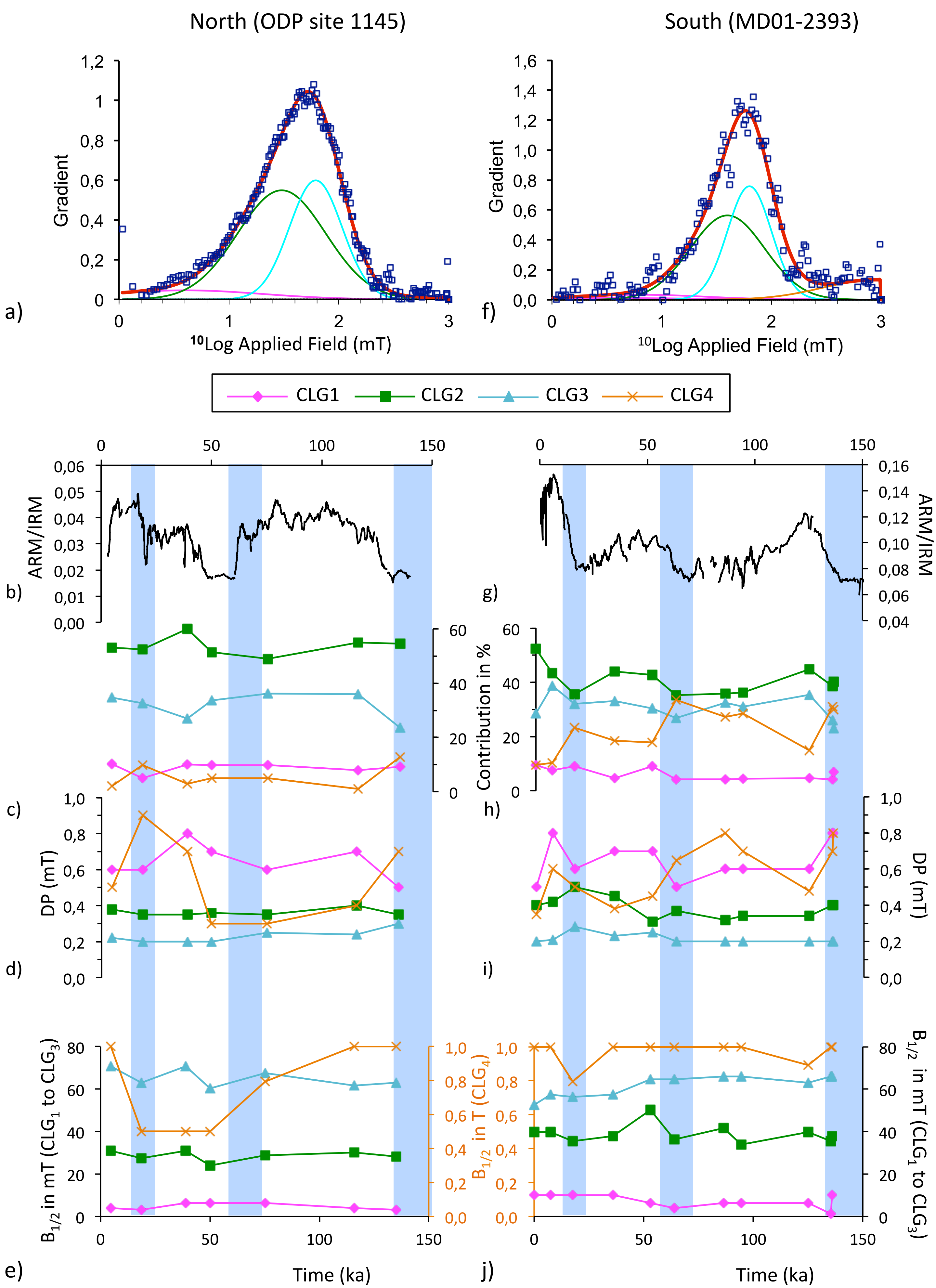
North (ODP site 1145)
South (MD01-2393)
Gradient
^{10}Log Applied Field (mT)
a)
f)
CLG1
CLG2
CLG3
CLG4
ARM/IRM
b)
g)
c)
h)
Contribution in %
DP (mT)
d)
i)
$B_{1/2}$ in mT (CLG_1 to CLG_3)
$B_{1/2}$ in T (CLG_4)
e)
j)
Time (ka)

Figure 9

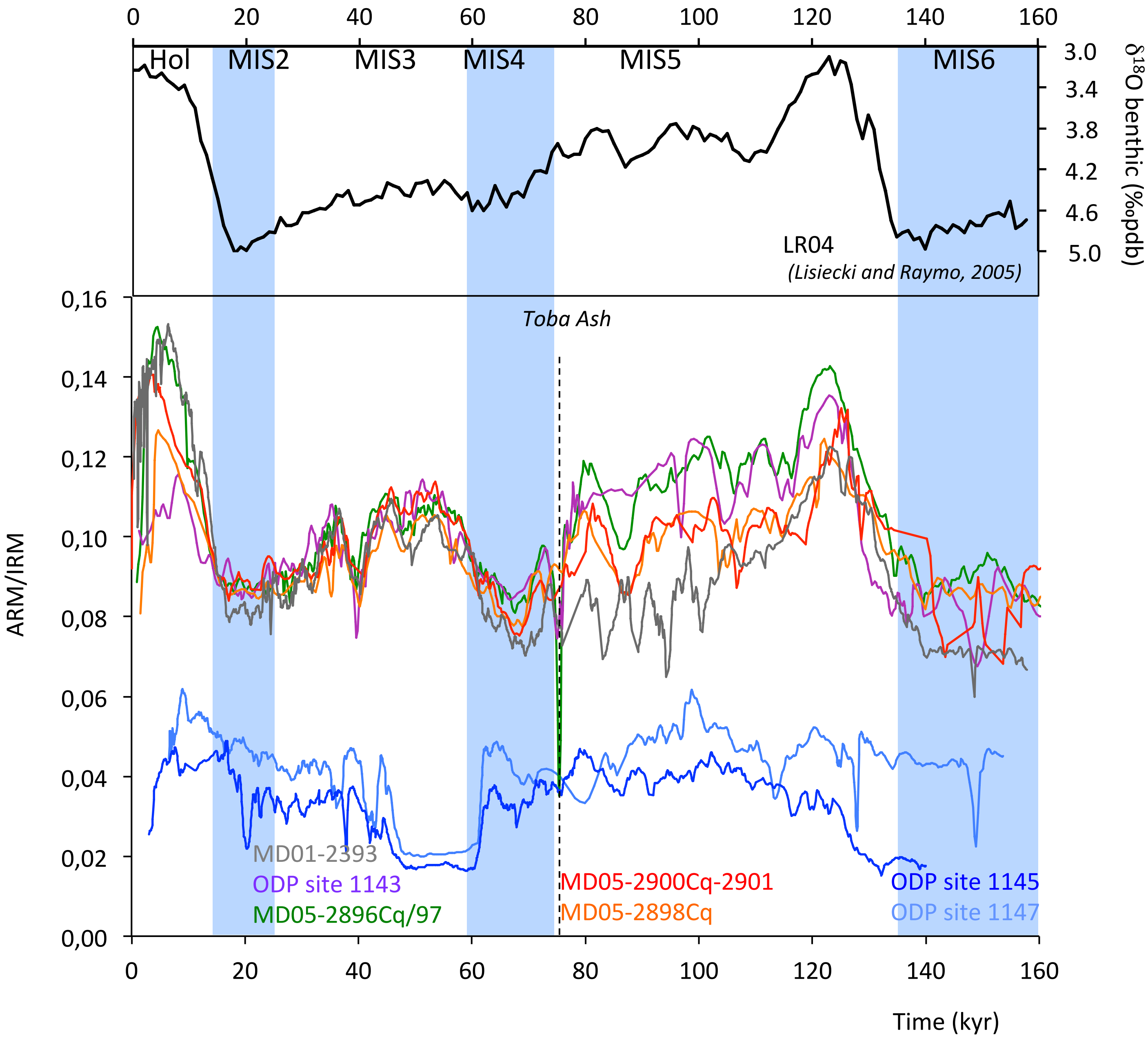
0
20
40
60
80
100
120
140
160
Hol
MIS2
MIS3
MIS4
MIS5
MIS6
3.0
3.4
3.8
4.2
4.6
5.0
δ18O benthic (‰pdb)
LR04
(Lisiecki and Raymo, 2005)
Toba Ash
0,16
0,14
0,12
0,10
0,08
0,06
0,04
0,02
0,00
ARM/IRM
MD01-2393
ODP site 1143
MD05-2896Cq/97
MD05-2900Cq-2901
MD05-2898Cq
ODP site 1145
ODP site 1147
Time (kyr)

Figure 10

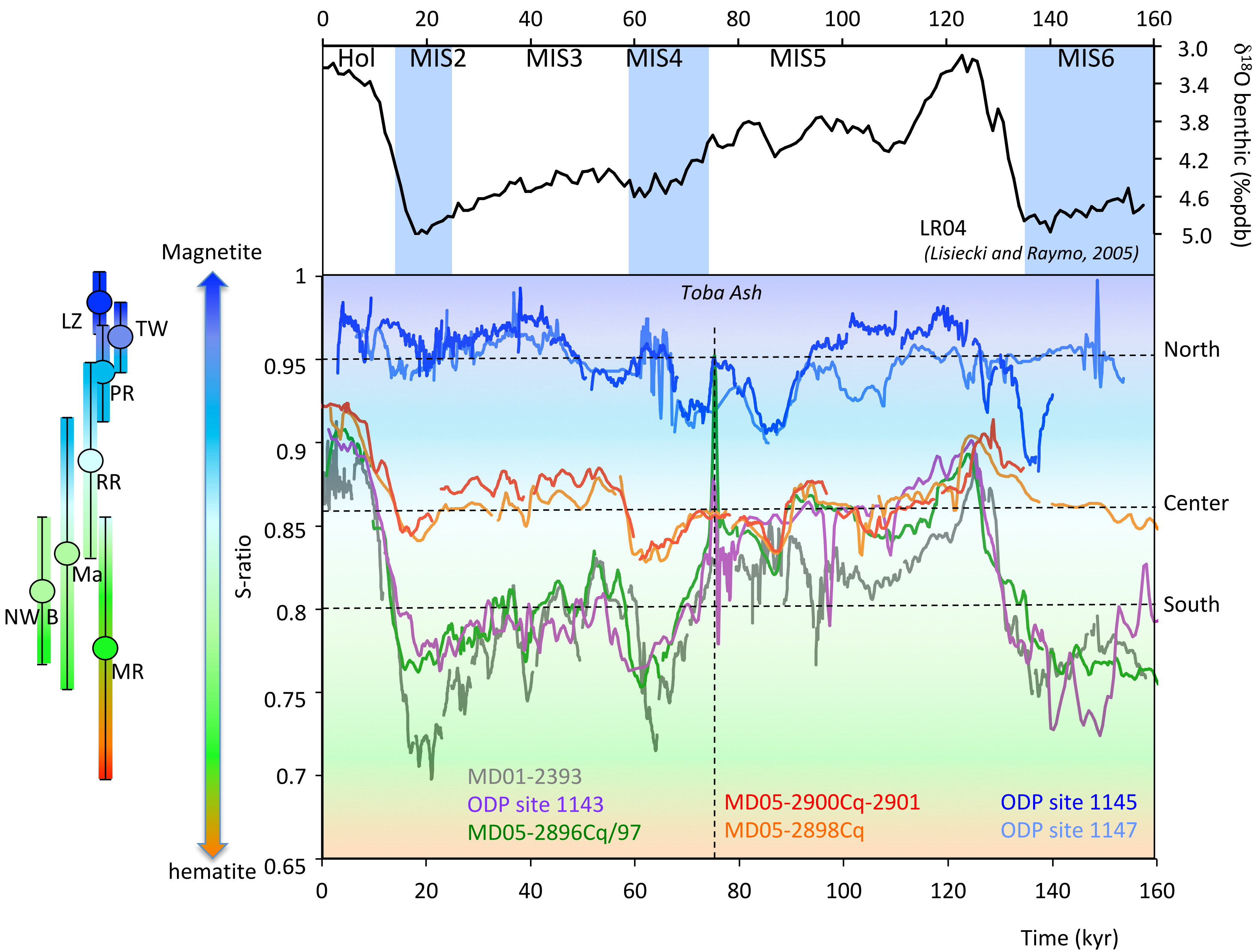
Hol
MIS2
MIS3
MIS4
MIS5
MIS6
LR04
(Lisiecki and Raymo, 2005)
δ18O benthic (‰pdb)
Toba Ash
North
Center
South
Magnetite
hematite
S-ratio
LZ
TW
PR
RR
Ma
NW B
MR
MD01-2393
ODP site 1143
MD05-2896Cq/97
MD05-2900Cq-2901
MD05-2898Cq
ODP site 1145
ODP site 1147
Time (kyr)

Figure 11

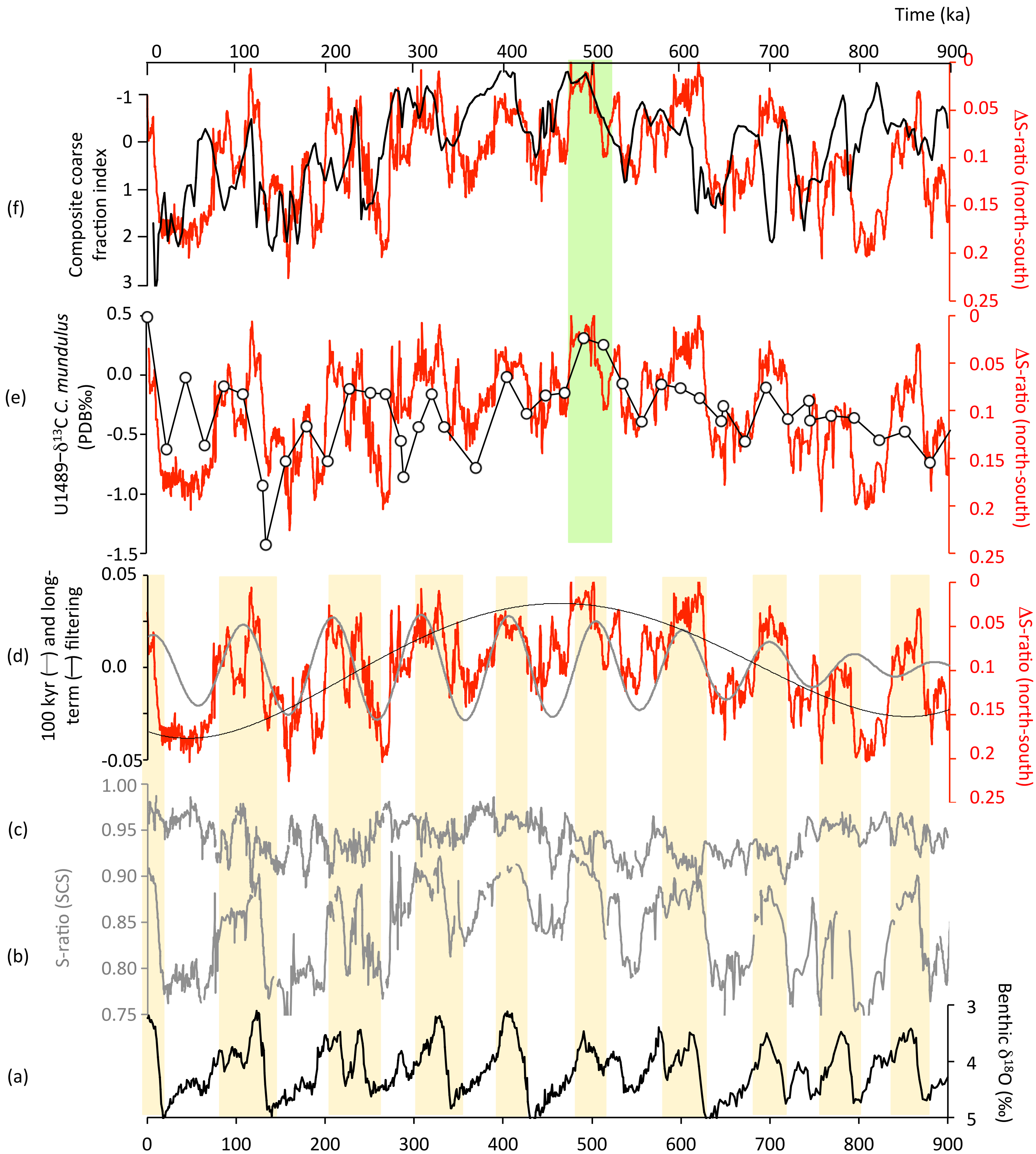

Time (ka)
Composite coarse fraction index
ΔS-ratio (north-south)
U1489–δ13C C. mundulus (PDB‰)
100 kyr (—) and long-term (—) filtering
S-ratio (SCS)
Benthic δ18O (‰)
(a)
(b)
(c)
(d)
(e)
(f)

Figure 12

Core	latitude (°N)	longitude (°E)	water depth (m)	mean sed rate (cm/kyr)	reference
North					
ODP 1145	19.58	117.63	3175	22.4	This study
ODP 1147	18.83	116.55	3245	20.5	This study
Center					
MD05-2898Cq	13.79	112.18	2395	5.8	This study
MD05-2900Cq/01	14.37	110.70	1455	9.6	This study
South					
MD01-2393	10.50	110.06	1274	23.8	This study
MD05-2896Cq/97	8.83	111.44	1657	8.5	This study
ODP1143	9.36	113.29	2772	8.7	This study
North					
10E203	20.58	118.38	2439	17.2	Zheng et al., 2016
ODP1144	20.05	117.42	2037	60 &120	Hu et al., 2012
STD111	20.02	116.36	1142	4.8	Yang et al., 2016a
ODP site 1146	19.46	116.37	2091	12	Kissel et al., 2003
MD12-3432	19.28	116.24	2125	12.6	Chen et al., 2017
Center					
PC24	17.4	113.7	3433	20	Ouyang et al., 2014b ; 2016
PC83	17.66	112.54	1917	6.6	Yang et al., 2009 ; Li et al., 2019
PC111	18.17	112.02	2253	6.6	Yang et al. 2009 ; Li et al., 2019
PC338	16.7	110.4	1349	5 to 50	Li et al., 2018
South					
YSJD-86GC	10.30	113.04	2651	6.3	Ouyang et al., 2014a
ODP site 1143	9.36	113.29	2772	7.5	Zhang et al., 2016

Table 2 : main magnetic parameters mentioned in this article and their respective meaning.

Parameter	Use/Meaning
A□/DC fields□□Al□□□na□□□□□Field, Direct Current bias field	**AF** : Incremented peak field steps are used to demagnetize any remanent magnetization. Superimposed to a biais **DC** field it is used to acquire the **ARM**, and at weak values, it is use to measure κ. **DC** : used for **ARM** and **IRM** acquisition.
κ: Volume low field magnetic susceptibility (ratio of induced magnetization to weak AF)	Concentration in para- and ferromagnetic (*s.l.*) fractions, more sensitive to very fine (super paramagnetism) and to coarse grains.
ARM_{0mT}: Anhysteretic remanent magnetization (acquired here by applying to 100 mT peak AF and 50µT DC field).	Remobilize the magnetic moments of the fine magnetite grains (<10 µm). Illustrates their concentration.
$IRM_{@1T}$: Isothermal remanent magnetization acquired stepwise by increasing fields up to 1T DC field.	Remobilize the magnetic moments of all the ferromagnetic particles sensitive to maximum 1T. Illustrates concentration and mineralogical mixtures.
$S\text{-ratio}_{0.3T}$ is calculated as the ratio of $IRM_{@1T}$ divided by the IRM acquired by a successive backfield of 0.3T	Mineralogy of the ferromagnetic particles (s.l): close to 1 for low coercivity minerals (magnetites, iron sulfides) and decreasing when high coercivity mineral content increases (hematite, goethite).
ARM/κ and **ARM/IRM**	Illustrate changes in magnetite grain size (increase with decreasing grain size). ARM/IRM ratio is more « pure » because only related to the ferromagnetism (*s.l*) and not biased by superpara- and paramagnetism.
MDF_{ARM}: Median destructive field of ARM. AF field to be applied to remove 50% of the total ARM	Illustrates the hardness of the mineralogical mixture in the low coercivity range. Varies with magnetic grain size (lower for coarser grains) of magnetite and iron sulfides.
$\%ARM_{@80mT}$: remaining ARM intensity (in percent with respect to the initial one) after applying peak AF at 80 mT	Illustrates the fraction of the low coercivity minerals not demagnetized by a 80 mT peak alternating field.
MDF_{IRM}: Median destructive field of IRM. AF field to be applied to remove 50% of the total IRM acquired at 1T	Illustrates the hardness of the mineralogical mixture present in the sample
$\%IRM_{@80mT}$: remaining IRM intensity (in percent with respect to the initial one) after applying peak AF at 80 mT	Illustrates the contribution to the total IRM of the high coercivity minerals which are not demagnetized at 80 mT (i.e. high coercivity minerals)
3-axes thermal demagnetization: stepwise thermal demagnetization of cubic samples which were submitted to 1T along one axis, then to 0.3 T to an orthogonal axis and finally to 0.1T along the third axis	Allows to characterize the thermal behavior (decay rate and characteristic Curie of Néel temperature) of each coercivity component and therefore to distinguish magnetites (typically 580°C) from iron sulfides(typically 350°C) in the low coercivity family and hematite (typically 690°C) from goethite (typically 120°C) in the high coercivity family.
Hysteresis parameters: Mrs, Ms, Hcr, Hc. After correcting for the high field slope. Mrs: remanent saturation magnetization; Ms: saturation magnetization; Hc: coercive force; Remanence curve with back fields : Hcr: remanent coercive force.	Used as magnetization ratio versus coercive forces ratio to determine the domain state of magnetites in turn related to magnetite grain sizes.
Anisotropy of the low field magnetic susceptibility	Gives access to the magnetic texture of the sediment. Defined by the orientation of the three axes of the mean ellipsoid (K1>K2>K3) and the shape parameters (F (=K2/K3) : foliation, L (=K1/K2) : lineation, P (=K1/K3) or Pj : degree of anisotropy)

CLG : decomposition of the IRM acquisition curves into cumulative Log-Gaussian Curves. Components characterized by : **%** (their contribution), $\mathbf{B_{1/2}}$ (the median acquisition field), **DP** (dispersion parameter)	Allows to discriminate the different coercivity components contributing to the IRM, in particular in the low coercivity range.

		Northern group		Central group		Southern group		
		ODP1147	ODP1145	MD05-2898Cq	MD05-2900Cq-01	MD01-2393	ODP1143	MD05-2896Cq-97
κ (10^{-6}SI)	mean ± 1σ	198.0 ± 38.8	236.6 ± 60.9	114.5 ± 17.9	112.8 ± 13.9	135.0 ± 23.0	101.7 ± 13.6	111.3 ± 14.2
	max/min	367.7 (114.6)	440.4 (104.4)	163.4 (77.2)	143.0 (79.4)	182.0 (41.0)	149.8 (74.9)	217.9 (72.6)
ARM (10^{-2}A/m)	mean ± 1σ	8.9 ± 2.7	7.8 ± 3.7	12.7 ± 2.4	13.3 ± 2.4	14.4 ± 2.8	10.9 ± 3.0	12.58 ± 3.2
	max (min)	15.9 (2.1)	15.9 (0.7)	20.1 (8.9)	21.1 (7.0)	23.1 (4.7)	18.8 (6.3)	19.9 (7.6)
$IRM_{@1T}$ (A/m)	mean ± 1σ	2.0 ± 0.5	2.2 ± 0.8	1.3 ± 0.2	1.3 ± 0.2	1.6 ± 0.3	1.1 ± 0.2	1.2 ± 0.2
	max (min)	4.2 (1.0)	5.9 (0.4)	1.6 (0.9)	1.8 (0.9)	2.1 (0.39)	1.8 (0.7)	2.3 (0.8)
S-ratio$_{0.3T}$	mean ± 1σ	0.95 ± 0.01	0.95 ± 0.02	0.86 ± 0.02	0.87 ± 0.02	0.80 ± 0.04	0.81 ± 0.04	0.81 ± 0.04
	max (min)	1.00 (0.90)	0.99 (0.88)	0.92 (0.83)	0.92 (0.83)	0.91 (0.70)	0.91 (0.72)	0.95 (0.75)
ARM/κ (10^2A/m)	mean ± 1σ	4.5 ± 1.0	3.1 ± 1.1	11.2 ± 1.8	11.9 ± 2.4	11.1 ± 3.5	10.7 ± 2.6	11.5 ± 3.5
	max (min)	7.1 (1.4)	4.9 (0.7)	16.1 (7.9)	19.2 (6.6)	22.9 (6.3)	17.4 (5.5)	23.1 (7.0)
100*ARM/IRM	mean ± 1σ	4.4 ± 0.8	3.3 ± 0.9	9.6 ± 1.0	10.0 ± 1.38	9.4 ± 2.07	9.9 ± 1.3	10.4 ± 1.6
	max (min)	6.2 (2.0)	4.9 (1.5)	12.7 (7.8)	14.1 (6.8)	15.3 (6.2)	13.5 (6.6)	15.2 (7.2)
HMD_{ARM} (mT)	mean ± 1σ	31.1 ± 1.3	29.91± 2.61	33.0 ± 1.03	33.2 ± 1.0	34.6 ± 1.2	35.4 ± 1.3	31.1 ± 1.6
	max (min)	33.9 (26.0)	38.0 (24.3)	35.4 (30.8)	36.0 (30.9)	36.7 (31.7)	37.9 (31.9)	38.3 (23.0)
%$ARM_{@80\ mT}$	mean ± 1σ	3.6 ± 0.6	3.1 ± 0.6	3.6 ± 0.2	3.7 ± 0.3	5.6 ± 0.3	5.1 ± 0.5	3.8 ± 0.4
	max (min)	4.7 (1.7)	5.1 (1.8)	4.4 (3.1)	6.3 (2.9)	6.3 (4.4)	6.2 (4.0)	4.8 (3.2)
HMD_{IRM} (mT)	mean ± 1σ	20.1 ± 1.3	18.1 ± 1.5	28.6 ± 1.7	28.1 ± 2.2	34.4 ± 4.0	34.3 ± 1.6	32.8 ± 1.0
	max (min)	25.4 (15.9)	27.1 (14.9)	36.8 (25.1)	32.5 (17.9)	41.1 (22.2)	38.6 (26.4)	35.6 (30.3)
%$IRM_{@80\ mT}$	mean ± 1σ	6.3 ± 1.1	5.9 ± 1.7	13.9 ± 1.2	13.2 ± 1.6	20.6 ± 3.9	18.9 ± 2.3	17.4 ± 2.8
	max (min)	10.4 (4.2)	13.1 (3.6)	18.3 (10.2)	16.1 (8.5)	28.6 (11.1)	23.9 (12.7)	22.2 (10.8)